Particle and Fibre Toxicology

RESEARCH

Open Access

In vitro inflammation and toxicity assessment of pre- and post-incinerated organomodified nanoclays to macrophages using high-throughput screening approaches

Todd A. Stueckle[1*], Jake Jensen[1], Jayme P. Coyle[1], Raymond Derk[1], Alixandra Wagner[2], Cerasela Zoica Dinu[2], Tiffany G. Kornberg[1], Sherri A. Friend[1], Alan Dozier[1], Sushant Agarwal[2], Rakesh K. Gupta[2] and Liying W. Rojanasakul[1]

Abstract

Background Organomodified nanoclays (ONC), two-dimensional montmorillonite with organic coatings, are increasingly used to improve nanocomposite properties. However, little is known about pulmonary health risks along the nanoclay life cycle even with increased evidence of airborne particulate exposures in occupational environments. Recently, oropharyngeal aspiration exposure to pre- and post-incinerated ONC in mice caused low grade, persistent lung inflammation with a pro-fibrotic signaling response with unknown mode(s) of action. We hypothesized that the organic coating presence and incineration status of nanoclays determine the inflammatory cytokine secretary profile and cytotoxic response of macrophages. To test this hypothesis differentiated human macrophages (THP-1) were acutely exposed (0–20 μg/cm^2) to pristine, uncoated nanoclay (CloisNa), an ONC (Clois30B), their incinerated byproducts (I-CloisNa and I-Clois30B), and crystalline silica (CS) followed by cytotoxicity and inflammatory endpoints. Macrophages were co-exposed to lipopolysaccharide (LPS) or LPS-free medium to assess the role of priming the NF-κB pathway in macrophage response to nanoclay treatment. Data were compared to inflammatory responses in male C57Bl/6J mice following 30 and 300 μg/mouse aspiration exposure to the same particles.

Results In LPS-free media, CloisNa exposure caused mitochondrial depolarization while Clois30B exposure caused reduced macrophage viability, greater cytotoxicity, and significant damage-associated molecular patterns (IL-1α and ATP) release compared to CloisNa and unexposed controls. LPS priming with low CloisNa doses caused elevated cathepsin B/Caspage-1/IL-1β release while higher doses resulted in apoptosis. Clois30B exposure caused dose-dependent THP-1 cell pyroptosis evidenced by Cathepsin B and IL-1β release and Gasdermin D cleavage. Incineration ablated the cytotoxic and inflammatory effects of Clois30B while I-CloisNa still retained some mild inflammatory potential. Comparative analyses suggested that in vitro macrophage cell viability, inflammasome endpoints, and pro-inflammatory cytokine profiles significantly correlated to mouse bronchioalveolar lavage inflammation metrics including inflammatory cell recruitment.

Conclusions Presence of organic coating and incineration status influenced inflammatory and cytotoxic responses following exposure to human macrophages. Clois30B, with a quaternary ammonium tallow coating, induced a robust

*Correspondence:
Todd A. Stueckle
tstueckle@cdc.gov
Full list of author information is available at the end of the article

cell membrane damage and pyroptosis effect which was eliminated after incineration. Conversely, incinerated nanoclay exposure primarily caused elevated inflammatory cytokine release from THP-1 cells. Collectively, pre-incinerated nanoclay displayed interaction with macrophage membrane components (molecular initiating event), increased pro-inflammatory mediators, and increased inflammatory cell recruitment (two key events) in the lung fibrosis adverse outcome pathway.

Keywords Nanoclay, Organic coating, Incineration, Silicates, In vitro models, High-throughput screening, Human lung cells, Mouse

Background

Research and development efforts of nanoclay-enabled technologies have steadily increased due to their use in advanced manufacturing of plastic nanocomposites [1–3]. Little is known, however, whether nanoclay exposure poses an occupational health risk across its lifecycle with known high exposure levels (up to 39.2 mg/m^3) [4–10]. Furthermore, in vitro nanoclay toxicity studies have been mostly restricted to epithelial cell responses with little effort to evaluate immune cell responses and immune system key events that lead to potential disease. There is a clear emerging need to further understand toxicological implications of nanoclay-enabled technologies across their life cycle to thus responsibly develop and implement safe nanoclay-based applications [6, 9].

One of the most popular nanoclays in advanced manufacturing, two dimensional (2D) smectite nanoclays (e.g. montmorillonite), possess a 2:1 phyllosilicate structure of an octahedral aluminum oxide sheet bounded by two tetrahedral silica oxide sheets on each side resulting in dimensions of 1 nm thick and hundreds of nm in length and width. Natural montmorillonite exists in a stacked mineral platelet morphology with hydrophilic properties. Addition of organic modifier coatings, such as quaternary ammonium tallow compounds (QACs), are used to improve nanoclay dispersion, rheology, barrier function, and thermal properties in composite materials [3, 11, 12].

Increased concern associated with ONC inhalation exposure in occupational settings along its lifecycle has driven pulmonary toxicity investigations. Inhalation of montmorillonite in miners resulted in a 'silicosis-like' lung pathology, most likely due to surface silica group reaction with lung tissue commonly associated with crystalline silica exposure [13, 14]. Addition of QAC coatings carries cell membrane and cytotoxicity hazards [15]. To address this, our group's previous work conducted thorough physicochemical characterization on a library of pre- and post-incinerated nanoclays. Cloisite Na, a pristine, uncoated montmorillonite possesses single and stacked platelet morphology with a silicate (Si–O–Si) and aluminate (Al–OH–Al) surface chemistry. Its organic coating derivative, Cloisite 30B, possesses similar characteristics but with an additional methyl, tallow, bis-2-hydroxyethyl, quaternary ammonium coating. Incineration of these two nanoclays resulted in I-CloisNa and I-Clois30B that possessed deformations of the OH linked to Al^{3-} and Mg^{2-} and increased presence of Al–O group. In addition, I-CloisNa still possessed Si–O–Si surface chemistry and a smooth surface consistent with amorphous silica. I-Clois30B surface chemistry analysis showed complete disappearance of the quaternary ammonium tallow coating with a heterogenous surface containing smooth amorphous, porous, or fused stacked platelet morphology suggesting that the presence of the organic coating caused partial retention of platelet structure [16, 17].

Comparative in vitro studies of pre-versus post-incinerated Cloisite® and Nanomer® ONCs largely reported that toxicity was influenced by the presence and type of the organic modifier, as well as incineration status in bronchial and small airway epithelial cell models [16, 18–20]. Uncoated nanoclays and ONCs caused monolayer integrity loss and apoptosis with different dose response curves, suggesting different potency or modes of action. ONC exposure caused enhanced particle uptake, inconsistent changes in reactive oxygen species (ROS), mitochondrial degeneration, and increased genotoxicity (i.e., micronuclei and DNA breakage) [15, 21–23]. Conversely, incinerated nanoclays produced minimal effects [16, 18–20]. Our group's in vivo pulmonary toxicity assessment of pre- and post-incinerated Cloisite® nanoclays [17], reported that ONC (Cloisite® 30B) exposure resulted in a low grade, delayed inflammatory response, consisting of increased macrophage and neutrophil infiltrations, elevated damage markers, and elevated pro-fibrotic cytokines at day 28. Conversely, Cloisite® Na^+ caused a robust inflammatory response with the same profibrotic signature as the ONC-exposed animals. Incinerated Cloisite® Na^+ elicited a transient inflammatory response while incinerated Cloisite® 30B produced a chronic inflammatory response, similar to aged crystalline silica (CS) [24]. Recent studies by Di Ianni et al. [25] reported that presence of QAC coating on bentonite decreased toxicity in exposed mouse lung; however, the same ONC caused potent in vitro epithelial and macrophage toxicity [26] which aligns with our assessments. Collectively, it

remains unclear what role pulmonary macrophages play in eliciting these observed in vivo effects. Very few studies on nanoclay exposure impacts to the immune system and chronic inflammation have been conducted but are critical since these responses to particle deposition typically drive lung pathology [27, 28]. At present, no thorough evaluation exists of how nanoclay exposure impacts lung macrophage cellular and inflammatory responses which can promote pulmonary disease. Defining lung macrophage and other major target cell's response to ONC exposure would identify those key events in an adverse outcome pathway (AOP) framework to improve screening strategies and inform risk assessment [29]. Furthermore, correlating in vitro response to in vivo metrics across particle types and characteristics can assist in placing in vitro models' screening role in an integrated testing framework. A recent review identified the need for systematic in vitro/in vivo extrapolation studies, identification of immunomodulatory biomarkers, and characterization of changes in toxic effect over the nanoclay lifecycle [15].

Past attempts at using in vitro models to predict in vivo effect following inhalation particle exposures has resulted in marginal success complicated by non-standardized test methods, particle kinetics, dosimetry, and differences in clearance mechanisms; however, recent improvements have occurred with use of the AOP paradigm [30–32]. Traditionally, in vitro studies with ultrafine particles to assess macrophage inflammatory and toxicity responses used LPS-primed macrophages [33]. Co-stimulation of macrophages with LPS allowed for priming of the inflammasome via NF-κB activation to evaluate the potential role of the NLRP3 inflammasome in driving inflammatory and toxicity response [28, 34]. Furthermore, it simulates a relevant occupational exposure (typically containing microbes and endotoxin) and mimics other priming signals (e.g. TNF) from other exposed cells [28]. However, a majority of lung particle exposures with animal models are typically conducted using sterile particle preparations under relatively sterile laboratory conditions [35, 36]. The absence of LPS allows for comparison of particle-induced inflammatory response across relatively sterile in vitro versus in vivo particle exposures and can assess whether a particle can activate the inflammasome in the absence of LPS. There is an inherent lack of in vitro studies that performed direct comparisons between LPS- and non-LPS stimulated macrophages and how that compares to the in vivo animal model response.

To address these issues, we conducted a study to investigate acute toxicity responses, several key events (KE) in the proposed 'substance interaction with the pulmonary resident cell membrane components leading to pulmonary fibrosis' AOP #173 [37], and potential underlying mechanisms for lung macrophages following occupationally expected exposure levels to pre- and post-incinerated organomodified nanoclay. The objectives were to (1) assess how differences in coating and incineration status determines differentiated macrophage response, and (2) correlate in vitro macrophage endpoints to in vivo responses. We hypothesized that the organic coating presence and incineration status of nanoclays determine the inflammatory cytokine secretary profile and cytotoxic response of macrophages. Herein, we report on particle characterization and macrophage toxicity and inflammatory responses to help further understand toxic effects observed in vivo.

Methods

Particle preparation and characterization

To screen and evaluate coating and incineration effects on nanoclays' potential for lung cell in vitro adverse outcomes, pristine (Cloisite® Na+; CloisNa) and an organomodified nanoclay (Cloisite® 30B; Clois30B) were purchased from Southern Clay Products (Gonzalez, TX). To model particles generated during end-of-life municipal incineration, both CloisNa and Clois30B were subjected to incineration during thermogravimetric analysis (900 °C for 100 min) and collected as incinerated nanoclays I-CloisNa and I-Clois30B as previously described [16]. Based on dry particle diameter and chemistry, heat inactivated crystalline silica (CS; Min-U-Sil 5; US Silica; Berkeley Springs, WV) was used as a benchmark particle for all studies. Non-freshly fractured (i.e. aged) Min-U-Sil 5 particle samples were dry heated at 180 °C for several hours to remove endotoxin and held at room temperature until used. Aged CS loses most of its silicon and siloxyl radicals compared to freshly fractured silica, but still retains silica structure and some inflammatory potential similar to pyrogenic silica [14, 24, 38]. All particle samples were UV sterilized and fully characterized for water and organic modifier content, surface chemistry, particle morphology, and elemental analysis by thermal gravimetric analysis, Fourier transform infrared spectroscopy, field emission scanning electron microscopy, and energy-dispersive x-ray spectroscopy, respectively, in previous publications [16, 17].

Stock particle suspensions (3 to 5 ml at 1 mg/mL) were made by adding sterile MilliQ water to known particle mass in sterile glass test tubes. Discrete sonication was used to disperse stock particle suspensions. Briefly, particle suspensions were lightly vortexed and sonicated three separate times (200.4 J/ml per run) with a cup horn (Sonics VibraCell VCX-750; Newton, CT) at 40% intensity immersed in cold water with a one-minute rest between sonications. This achieved a total critical sonication energy (DSE_{cr} = 601.2 J/ml) needed to reach relatively

stable suspensions of dispersed particles with lowest agglomerate formation [39]. Particle suspensions were immediately serially diluted in Roswell Park Memorial Institute + 10% FBS (RPMI) THP-1 cell culture medium. Media density, viscosity, and refractive index (Additional file 3: Table S1) were determined using a volumetric flask with balance, viscometer, and a refractometer following previously described methods (n = 3 independent experiments) [40] and were used as input parameters to calculate hydrodynamic diameter via dynamic light scattering analysis (DLS). Effective density (ρ_{EV}) of each particle (0.1 mg/ml) in medium was measured using particle density, packed pellet volume, medium density, and theoretical stacking factor (SF = 0.634) as previously described (n = 3) [40, 41]. Soluble endotoxin in sonicated stock suspensions (n = 3) were determined with the Pierce LAL chromogenic method as previously described (ThermoFisher Scientific, Waltham, MA) [17].

DLS, particle dispersity index (PdI), and zeta potential analyses using a Zetasizer Nano ZS (Malvern, Malvern, UK) were also performed for each particle in water and culture medium described below. DLS analysis calculates hydrodynamic radius for low aspect ratio three dimensional particles, hence, it is not a reliable technique for determining 2D particle size in suspension [42]. Here, DLS was performed to make relative size comparisons among particle types. Particle suspension pH of each particle in medium was determined (n = 3) using a standard pH meter (Accumet Model 50, Fisher Scientific). Immediately after sonication, particles were diluted to 100 µg/mL and analyzed for size and zeta potential using a Universal Dip Cell (Malvern). Three runs per experiment and three independent experiments were performed. Since Clois30B particles were observed to re-agglomerate and fall out of suspension following dispersion in water [17], only the first runs off of each experiment were used for hydrodynamic diameter and PdI analyses. Likewise, incinerated nanoclay particles showed low suspension stability, hence, a similar analysis approach was taken. Values from each run were averaged (n = 3).

X-ray diffraction

X-ray diffraction (XRD) analysis was used to assess spacing between nanoclay platelets and confirm the absence of platelet spacing in incinerated particle samples. For Bruker XRD analyses, dry powder samples were placed on glass slides using a thin layer of vacuum grease. Specifically, the powders were placed on top of the vacuum grease with excess powder being shaken off; this process was repeated until a thin layer of the powdered samples was obtained. The glass slides containing the samples were then mounted onto the sample holder via double sided tape and the Bruker D8 Discovery (Madison, WI) was aligned. Diffraction was obtained (n = 3) in the 2°–9.5° 2θ range at increments of 0.02° at a scan speed of 10 s/step. A Cu-kα1 8047.2 eV radiation source at 40 kV and 40 mA was used. Basal spacing was determined by Bragg's equation:

$$n\lambda = 2d\sin\theta,$$

where n is an integer, λ is the wavelength of the X-ray radiation (0.1546 nm), d is the spacing between lattice planes, and θ is the measured diffraction angle. The peak locations were determined via Match (Crystal Impact, Bonn, Germany).

Next, to evaluate crystallinity of pre-incinerated nanoclay and compare incinerated nanoclay structure to that of CS, XRD via an X'Pert Pro (Malvern PANalytical) was conducted by placing samples on glass slides in a thin, even layer which were then mounted in the sample holders. Diffraction was obtained (n = 3) in the 5°–100° 2θ range at a scan speed of 10 s/step. A Cu-kα1 8047.2 eV radiation source at 45 kV and 40 mA was used. XRD patterns were identified using X'Pert HighScore (PANalytical) or the RRUFF Project database.

Cell culture

THP-1 monocytes were acquired from ATCC (Manassas, VA) and were cultured in ATCC-recommended Roswell Park Memorial Institute (RPMI) 1640 formulated medium supplemented with 10% fetal bovine serum (FBS), L-glutamine, 0.05 mM β-mercaptoethanol, 1 mM sodium pyruvate, and 1% penicillin/streptomycin (Sigma-Aldrich, St. Louis, MO). THP-1 cells were chosen as a suitable model based on its standardized use as a human macrophage model for particle and fiber toxicology studies [43]. Monocyte stock cultures were maintained between 2 to 8×10^5 cells per mL for a maximum of one month in CellStar flasks (Fisher Scientific). For all microplate assays, monocytes between 4 and 10 passages were seeded at 2×10^4 cells per well in a black-walled clear bottom tissue culture-treated 96-well plate (Corning, Corning, NY) in the presence of 1α, 25-dihydroxy-Vitamin D_3 (Sigma-Aldrich) at 150 nM to differentiate into adherent cells for 48 h. Next, attached cells were exposed to 10 nM of phorbol, 12-myristate, 13-acetate (Sigma-Aldrich) for 12 h to complete differentiation. This protocol has been shown to minimize cell clumping and maximize cell response to stimuli [43, 44]. Confirmation of differentiated THP-1 macrophages was conducted (see Additional file 2). For particle exposure, attached differentiated THP-1 cells were briefly washed with warm (37 °C) phosphate-buffered saline (PBS) and then co-exposed with or without 10 ng/mL lipopolysaccharide (LPS; Sigma-Aldrich) and test particles at the reported particle dose ranges (described below) in quadruplicate.

All water-soluble tetrazolium salt-1 (WST-1) and lactate dehydrogenase (LDH) assays in this study were performed in Falcon tissue culture-treated 96-well plates.

Field emission scanning electron microscopy (FESEM) and transmission electron microscopy (TEM) analyses

FESEM imaging analyses were conducted to ascertain particle size and morphology in water and cell culture medium preparations following previously described procedures [17]. Briefly, each sonicated particle stock suspension (n = 3) was diluted into vehicle at 25–100 µg/mL, filtered onto polycarbonate filter, gold/palladium sputter coated, and imaged with a S-4800 FESEM (Hitachi, Tokyo). Particles in complex medium were diluted to 25 µg/mL with sterile filtered MilliQ water to reduce medium interference with particle imaging. 20–30 representative images were taken to compare to dynamic light scattering analyses. Length and maximum width for each located particle in digital FESEM images were measured in ImageJ v1.52 (NIH) with n = 104–437 per particle.

To qualitatively ascertain particle uptake and intracellular location into exposed cells, THP-1 cell were seeded at 5×10^5 in 6-well plates overnight following published method [45]. Next, cells were exposed to each particle type at 0.6 µg/cm^2 for 24 h in duplicate, rinsed with saline wash, trypsinized, collected, and centrifuged to collect a pellet of exposed cells. The pellet was resuspended in fixative, processed, blocked, sectioned, mounted on copper TEM grids, and imaged with a TEM (JEOL 1400, Tokyo, Japan). 20–30 images were taken to evaluate cellular uptake potential for each particle. Three independent experimental replicates were performed.

To confirm particle uptake prepared TEM grids were stabilized by carbon evaporation by coating them with a 20 nm carbon film using a Leica ACE 600 carbon coater. This stabilization was required for unsupported thin sections to withstand an exposure to the 200 keV Schottky field emission electron beam utilized in the NIOSH JEOL 2100F analytical TEM-STEM (scanning transmission electron microscope). EDS (energy dispersion spectroscopy) analysis with a silicon drift x-ray detector (Oxford Aztec) was performed in the STEM operating mode with a 1 nm electron probe. This operating mode was used to enable the precise analysis of a nanoparticle utilizing drift correction. The STEM operating mode is equipped with bright and dark field detectors with the EDS system allowed to access the dark field detector for compositional analysis of materials. The EDS system is capable of both point and 2-dimensional atomic compositional analysis to produce mapping of the spatial distributions of different atomic species. Intra-cellular nanoparticles were initially located using a low voltage (100 keV) TEM optimized for biological imaging. These intra-cellular nanoparticles were then relocated in the NIOSH analytical TEM/STEM system using micrographs from the previous TEM observations by matching the morphology of identified cells and their nuclei.

WST-1 and LDH assays

Differentiated THP-1 cells were seeded at 2×10^4 cells per well as described above. Next, cells were exposed to each freshly sonicated particle in 200 µl at 0.02–20 µg/cm^2 (0.032–32 µg/ml) in quadruplicate for 24 h. The highest in vitro dose represented the OSHA permissible exposure limit (5 mg/m^3) for respirable particles not otherwise regulated assuming an exposure of 45 year working lifetime, 240 days per year, and other particle and lung parameters [46]. THP-1 cells were exposed to LPS or LPS-free medium to ascertain their cell activity in the presence and absence of a robust inflammatory response. 1% Triton-X (Sigma-Aldrich) applied to cells for 2 h served as a positive 100% cytotoxicity control. Following exposure, plates were centrifuged at 1000 rpm for 5 min and the top 100 µl of supernatant was collected for lactate dehydrogenase (LDH) assay to measure cytotoxicity (Roche, Indianapolis, IN) according to manufacturer's instructions. Next, 10 µL of WST-1 reagent (2-(4-iodophenyl)-3-(4-nitrophenyl)-5-(2,4-disulfophenyl)-2H-tetrazolium; Roche) was added to the remaining medium with cells and incubated for 2 h to measure cell viability. Absorbance of each well was read on a microplate spectrophotometer (SpectraMax Plus 384, Molecular Devices) at 490 and 450 nm for LDH and WST-1 assays, respectively. LDH interference assay was conducted by incubating 2.5 mU/well of purified LDH-A (Millipore-Sigma) in medium in the presence of serially diluted particle for 24 h. Absorbance values were corrected in medium only values and % interference calculated (Additional file 3: Table S2). All values for each particle and medium type were corrected with interference values. Four independent experimental runs were performed.

Quantitative high-throughput screening analyses

Cells were seeded in black 96- or 384-well plates with clear bottom (Corning) at 2×10^4 cells/well and exposed to applied doses of 0–20 µg/cm^2 for each particle. A two-way 5 × 8 complete design was used for each discrete time point with a minimum of quadruplicate replicates per treatment. A mass per unit alveolar surface area dose metric was used to directly compare in vitro responses to in vivo pulmonary exposure responses [17]. Our in vivo study found that aspirated nanoclay and CS primarily deposited in the terminal bronchioles, alveolar ducts, and surrounding alveoli. The low (30 µg/mouse) and high (300 µg/mouse) dose in vivo exposures in a 500

cm^2 alveolar epithelial surface area in a mouse lung [47] would equal an applied in vitro dose of 0.06 and 0.6 µg/cm^2, respectively. This approach has limitations since it assumes 100% deposition of the aspirated mass and that alveolar macrophages are homogeneously dispersed throughout the deep lung. Thus, careful interpretation of in vitro to in vivo correlations must be performed.

THP-1 cells were exposed for 0–24 h and then assayed using quantitative HTS screening approaches via multiplex fluorescent automated imaging at 4×, 10×or 20×magnification on an ImageXpress Micro XLS (Molecular Devices, Sunnyvale, CA) possessing a CMOS 16-bit digital camera. Endpoints and the multiplex fluorescent staining used are described in Table 1 and below. Assays were conducted based on modifications to previously described standardized methods or strictly following fluorescent dye manufacturers' protocols [48, 49]. If recommended by dye manufacturer or to reduce high background signal, stained cells were washed with 37 °C fresh culture medium then imaged in clear Fluorobrite DMEM (ThermoFisher). Automated HTS imaging using one, four, or nine image replicate sites per well were taken for 4 ×, 10 ×, and 20×magnifications, respectively. HTS image analysis was conducted as previously described [18] using several application models in MetaXpress v6.2 which allows for quantification of cell-specific fluorescent intensities and can remove non-cell specific staining and background interference [18, 50]. Particle-only control wells with same concentrations and dyes were imaged and used to subtract positively labeled particles in each assay. Following image quality control criteria, each measured parameter from each cell was averaged within site, replicate sites averaged within well, and exported to Excel for statistical analyses.

Live cell scoring using propidium iodide (PI) nuclear exclusion as a marker for live cells was used as a corroborative measure of cytotoxicity and proliferation with the WST-1 assay following pre- and post-incinerated nanoclay particle exposure. Following particle exposure, a 10×concentration of Hoescht 33,342 (ThermoFisher) and PI (ThermoFisher) was added to exposure medium for a final working concentration of 1 µM Hoescht and 5 µg/ml PI. Triton-X at 0.1% acted as a positive cell death control while retaining the overall cell plasma membrane intact. Cells were incubated for 30 min at standard culture conditions (37 °C and 5% CO_2 humid air) followed by imaging at 10×magnification with 4 sites per well. Nuclei and PI were imaged with DAPI and Cy5 filters, respectively. Number and percentage of live and dead cells per site were determined and averaged per well within Multi-wavelength Cell Scoring (MCS) application module in MetaXpress, and then corrected for both unexposed and positive cytotoxicity controls to calculate percent survival. Data represent four technical replicates across a minimum of three independent experiments.

JC-1 stain (ThermoFisher) was used to measure changes in mitochondrial membrane potential (MMP) following particle exposure by calculating the ratio of red (J-aggregates, healthy mitochondria) to green (monomers, depolarized mitochondria) integrated intensities of labeled mitochondria in each cell. Following exposure, live cells were stained with a 20×dye cocktail to achieve a working concentration of 1 µg/ml JC-1 and 1 µM Hoescht. Cells were incubated for 15 min as described above followed by careful removal of treatment medium, one wash in warm serum-free medium, and addition of 100 µl of warm medium per well for imaging. Positive control for MMP depolarization consisted of cells exposed to 10 µM valinomycin 30 min prior to imaging. J-aggregates and monomers were imaged with TRITC and FITC standard filters while nuclei were imaged with DAPI filter at 20×magnification with 9 sites per well. TRITC and

Table 1 Key event screening approach in THP-1 macrophages following pre- and post-incinerated organomodified nanoclay exposure

Key event	Stains[a]	Fluorescent channels
Live/dead	Propidium Iodide	DAPI, Cy5
Mitochondrial membrane potential	JC-1	DAPI, FITC, Cy3
Reactive oxygen species	CellRox Green	DAPI, FITC
Cell membrane damage[b]	LDH	n/a
Cell metabolism[b]	WST-1	n/a
Lysosome damage	Magic Red Cathepsin B	DAPI, Cy5
Caspase 1	FAM-FLICA Caspase 1	DAPI, FITC
Caspase 3/7	Cell Event/Propidium Iodide	DAPI, FITC, Cy5
Inflammation response	Multiplex Luminex beads	n/a

[a] All HTS assays, except WST-1 and LDH contained Hoechst 33,342 as a nuclear stain

[b] Non-HTS traditional assays

FITC integrated intensities of each cell were determined per site and averaged per well in MCS. Data represent four technical replicates across a minimum of three independent experiments.

Screening for changes of intracellular reactive oxygen species (ROS) following particle exposure was performed with CellRox Green (ThermoFisher Scientific) staining. Prior to staining, 100 μM of menadione (MP Biomedicals) was applied to four replicate wells for 30 min to serve as positive ROS controls. Following particle exposure cells were treated with 10 × dye cocktail with target concentrations of 5 μM CellRox Green and 1 μM Hoescht 33,342. Cells were incubated for 30 min as described above, centrifuged to pellet unattached cells, and immediately imaged, or fixed in 4% formaldehyde for 15 min at room temperature, washed, and held in sterile PBS for later imaging. Nuclei and intracellular ROS were imaged with DAPI and FITC filters at 10 × or 20 × magnification with 4 or 9 sites per well, respectively. Integrated intensity of the FITC signal was averaged for each site and within well in MCS, then averaged for treatment groups. Attempts to quantify ROS in LPS-stimulated THP-1 cells were unsuccessful due to fluorescent signal above maximum threshold, therefore only non-LPS stimulated THP-1 cell data is reported. Data represent four technical replicates across a minimum of three independent experiments.

Magic Red Cathespin B staining (Immunochemistry) was employed to assess lysosome damage, an initiation step in NLRP3 inflammasome activation, following the manufacturer's instructions. Following exposure cells were directly stained with a concentrated stock solution to achieve a working concentration of 5% Magic Red dye with 1 μM Hoescht 33,342 in cell culture medium. Cells were incubated under normal culture conditions for 1 h. Nigericin exposed cells (10 μM for 4–24 h) served as a positive control during assay development with maximum staining occurring between 16 and 24 h exposure. Cell plates were briefly centrifuged at 125×*g* for 5 min and immediately imaged at 20 × magnification with 9 sites per well. Integrated intensity of the Magic Red stain was determined for each cell and averaged within site in MCS. Data represent four technical replicates across a minimum of three independent experiments.

Caspase 1 FLICA (Immunochemistry), CellEvent Caspase 3/7 (Molecular Probes), and propidium iodide screening assays were used to distinguish between pyroptosis, apoptosis, and necrotic cell death in differentiated macrophages following nanoclay particle exposure following manufacturers' protocols. For Caspase 1 assay after 4–12 h particle exposure, cell plates were centrifuged for 125×*g* for 5 min and then each well gently aspirated with a multi-channel pipette. A 1:150 dilution of FLICA dye in serum-free medium was applied to each well followed by 1 h incubation at standard culture conditions. Cells were then centrifuged, media with dye gently aspirated, and washed with warm PBS. Cells were incubated again in serum-free medium with 10 μg/ml PI and 1 μM Hoescht 33,342 for another hour to remove unbound FLICA. Plates were then centrifuged, washed, and immediately imaged in 100 μl of warm PBS at 37 °C in the IXM system. Nigericin exposed cells (10 μM for 4–24 h) served as a positive control during assay development with maximum staining occurring between 16 and 24 h exposure. Cells were imaged with DAPI, FITC, and Cy5 filters at 20 × magnification with 9 sites per well. First, cells were identified as possessing intact membrane (nucleus PI−) or leaky membranes (nucleus PI+) using MCS. FLICA integrated intensity was calculated for each cell, averaged within site, and averaged among wells. Next, cells with no or low (< 20% unexposed cells) FLICA integrated intensity and PI-, high FLICA (> 20% control) with PI-, high FLICA with PI+, and no FLICA and PI+ were scored as healthy, early pyroptosis, late pyroptosis, and necrosis, respectively.

For Caspase 3/7 assay, a 10 × concentrated staining cocktail containing CellEvent, propidium iodide, and Hoescht 33,342 was prepared in warm PBS containing 5% fetal bovine serum. The dye cocktail was delivered to each well to reach 3 μM, 10 μg/ml, and 1 μM working concentrations for each dye, respectively, after 4–6 h following exposure. Stained cells were incubated for 30 min in standard culture and centrifuged at 125×*g* for 5 min to pellet detached apoptotic and necrotic cells. Cells were immediately imaged with DAPI, FITC, and Cy5 filter sets. First, cells were identified as possessing intact membrane (nucleus PI-) or leaky membranes (nucleus PI+) in MCS. Procedures to determine CellEvent intensity as a function of particle × dose and percentage of cells within healthy, early apoptosis, late apoptosis, and necrosis followed those described for Caspase 1 assay. Four independent experimental runs were performed.

ELISA and western blot analysis

To assess macrophage acute inflammatory signaling, THP-1 cells were seeded at 1.5×10^5 per well and differentiated in 6-well plates as described above. Cells were then exposed to each particle (0, 0.06, 0.6 or 6 μg/cm^2) in the absence or presence of LPS for 24 h (n = 3). Next, plates were centrifuged at 125×*g* for 5 min to remove cell debris and the conditioned medium was collected and temporarily stored at − 80 °C. To evaluate release of damage-associated molecular pattern molecules (DAMPs) as evidence of the molecular initiating event (MIE) in the lung fibrosis AOP, thawed and diluted aliquots of non-LPS exposed supernatants were assayed for

IL-1α via ELISA (R and D Systems) and ATP via firefly luciferase bioluminescence assay (ThermoFisher) following manufacturers' protocols. Tetramethylbenzidine optical density and luminescent intensities were quantified on a spectrophotometer (Spectramax) and H1 Synergy (Biotek, Winooski, VT), respectively (n = 3).

Next, to evaluate release of pro-inflammatory mediators as the first KE in the AOP, thawed samples were assayed in duplicate using a multiplex inflammation chemokine/cytokine assay using magnetic beads (R and D Systems, Minneapolis, MN) following the manufacturer's protocol. In addition to acute inflammation response targets used for the in vivo study, we expanded the multiplex array to characterize differentiated THP-1 cell inflammation response following pre- and post-incinerated nanoclay exposure. Samples were assayed for each target's concentration via a Luminex system (MilliporeSigma, Burlington, MA) using serial dilution of the manufacturer's standards. Data were averaged between replicates and tested for differences among treatment groups. Lastly, data were transformed to $\log_2$ fold change values, globally Z score normalized within targets and treatments, feature scaled between + 3 and − 3, and plotted in a heat map using 2 factor hierarchical clustering analysis in SAS JMP v13 (SAS Institute, Cary, NC).

Gasdermin D was recently identified as the key effector protein for inflammasome-mediated pyroptosis since its N-terminus cleavage product (GSDMD-NT) by caspases forms membrane pores [51]. To assess macrophage pyroptosis induction by nanoclays, differentiated THP-1 cells in 6-well plates at 1.5×10^6 cells, co-exposed with LPS, were exposed to 0–20 μg/mL of each particle for 24 h in duplicate. A positive control for GSDMD cleavage in THP-1 cells was performed by incubation of THP-1 cells with 100 ng/mL LPS for 4 h, followed by a 2-h incubation with 15 μM nigericin. Next, cells were placed on ice for 5 min, rinsed with cold PBS, and lysed with cell lysis buffer (Invitrogen, Carlsbad, CA) containing protease cocktail inhibitor and PMSF. Cell lysates were scraped with a rubber policeman, collected into Eppendorf tubes, briefly sonicated, and allowed to complete lysis for 20 min on ice prior to storage at − 80 °C. Total protein concentrations were measured using BCA assay. Three independent experiments were conducted.

GSDMD-NT expression analysis was conducted using a SimpleWes protein expression system (ProteinSimple, San Jose, CA) using capillary electrophoresis and antibody incubations. Briefly, 1 μg of each protein lysate from nanoclay-exposed differentiated THP-1 cell was placed onto loading plate along with gel matrix solutions, immobilization buffers, 1:50 dilution primary Gasdermin D antibody (Novus Biologicals, Littleton, CO), 1:200 dilution of secondary anti-rabbit streptavidin horseradish peroxidase (HRP) antibody (Cell Signaling Technology, Danvers, MA). Protein in the capillaries was separated by size via gel electrophoresis followed by incubation with primary and secondary HRP antibodies. Digital imaging of chemiluminescent bands was performed and bands at 55 and 38 kD were quantified via Compass software (Protein Simple, Wallingford, CT). Change in GSDMD-NT were calculated as percent band intensity of the cleaved product of total cleaved and full length GSDMD band intensities (n = 3).

Animals

All animal data herein was collected as part of our previous in vivo study that reported on the pulmonary inflammatory and histopathological effects following oropharyngeal aspiration of a single bolus of 30 μg and 300 μg/mouse of each particle to male C57Bl/6J mice (Jackson Labs, Bar Harbor, ME) [17]. All procedures for this animal study were reviewed and approved by the CDC-Morgantown Institutional Animal Care and Use Committee and were conducted in an AAALAC-accredited facility.

Cytospin analysis

To qualitatively evaluate in vivo uptake of each particle type by alveolar macrophages and approximate intracellular location, phase contrast imaging of fixed cells from bronchoalveolar lavage (BAL) was conducted (n = 8) as previously described [17]. Briefly, a cannula was inserted into the esophagus of euthanized mice, attached to a sterile syringe, then followed by the addition 0.8 ml of ice cold phosphate-buffered saline to the entire lung. Mild compressions of the chest were performed as fluid was collected into the syringe. Lavage was performed 4 times and centrifuged to pellet collected cells. BAL cells were resuspended in saline and counted. Collected BAL cells were immobilized via Cytospin, fixed and stained with a HEMA3 stain kit (Fisher Scientific), and imaged with a Leica DM2500 equipped with an Olympus DP73 digital camera. Images were evaluated for intracellular and extracellular particulate and compared to both in vitro TEM images and in vivo stained histological sections of lung.

In vitro–in vivo *correlation analyses*

To ascertain whether in vitro THP-1 macrophage response to nanoclay particle exposure aligns with lung inflammation metrics from in vivo models, several sets of correlation analyses were conducted. Three different in vitro dose equivalents of the in vivo dose were used to assess the robustness of correlating the THP-1 macrophage effects to in vivo inflammatory metrics. THP-1 macrophage cell viability, in both the presence

and absence of LPS, at 0.06 and 0.6 μg/cm^2 (dose equivalent), 0.2 and 2 μg/cm^2 (threefold dose equivalent), or 0.6 and 6 μg/cm^2 (tenfold dose equivalent) for each particle was correlated to BAL cell differentials in 30 and 300 μg-exposed male C57Bl/6J mice (with 500 cm^2 lung surface area) at Day 1 and Day 7 from our previous study [17]. Next, cathepsin B intensity, gasdermin D cleavage level, and IL-1β were correlated to BAL cell differentials. Next, each particle's 16 inflammatory cytokine profile in THP-1 macrophages, in both the presence and absence of LPS, was correlated to the same corresponding cytokines for each corresponding dose level (0.06 μg/cm^2 and 30 μg/lung; 0.6 μg/cm^2 and 300 μg/lung; or 6 μg/cm^2 and 300 μg/lung) at Day 1 and Day 7 post-exposure in vivo time point in C57Bl/6J-exposed mice [17]. Lastly, each cytokine level in THP-1-exposed cells was correlated to BAL corresponding levels across particle types. Correlation analyses are described below.

Statistical analyses

Dose–response curves were modeled and fitted using the "drc" package [52] using the R v. 3.6.1 statistical program (R Foundation for Statistical Computing, Vienna, Austria). The effective dose to cause a 50% reduction in the measured response (ED_{50}) compared to the control and associated estimate standard deviation were derived from fitted models using the "drc" package. ED_{50} values that exceeded the highest dose test (20 μg/cm^2) were designated as > 20 μg/cm^2. Statistical comparisons between modeled ED_{50} were performed via a two-sample *t* test. Where appropriate, defined ED_{50} value comparisons against particle effective doses designated as > 20 μg/cm^2 were performed using a one-sample t-test, wherein the null value was set to 20. Differences in particle characteristics in media were determined by one-way analysis of variance (ANOVA). To determine differences in macrophage responses among treatment groups, 2-way ANOVAs were conducted. All data were evaluated for variance homoscedasticity and normal distribution of residuals ($\alpha = 0.05$) prior to conducting an ANOVA. Data not meeting these ANOVA assumptions were tested with a Wilcoxon or Kruskal–Wallis test. If ANOVAs indicated a difference, Tukey–Kramer HSD post-hoc tests were run to identify those treatment groups different from others. For correlation analyses, all THP-1 cell and BAL mouse data were transformed to fold change compared to their respective unexposed controls and then log-transformed for data normalization. Pearson's coefficient correlation analyses were run for data with normal distributions to assess potential in vivo predictive value of these in vitro screening approaches. Spearman's coefficient correlation analysis was performed for data sets without a normal distribution. If a particle treatment elicited a low number of significantly different cytokines compared to unexposed cells, correlation analysis was not conducted. All other data were analyzed with JMP SAS (version 13) software.

Results

Physicochemical characterization of pre- and post-incinerated nanoclays

All particle characteristics in dry and culture medium suspension are summarized in Table 2. XRD and FESEM analyses indicated that both CloisNa and Clois30B were montmorillonite with dioctahedral structure and stacked platelet morphology. Clois30B displayed increased basal spacing compared to CloisNa indicative of the organic QAC coating (Fig. 1A, B; Table 2). Dispersed CloisNa in RPMI medium exhibited single or stacked platelet morphology similar to that observed in water (Fig. 2; Additional file 1: Figure S1). CloisNa showed the significantly smallest mean length and width (medians 294 and 174 nm) compared to all other particles (Additional file 3: Table S3) with DLS size data matching FESEM data. CloisNa dispersed well (i.e. low PdI) and possessed the lowest ρEV of all particles tested (Table 2). Clois30B exhibited a range of size distributions, compared to CloisNa, and consisted of small sub-micron or large single micron stacked platelet morphology with size median of 304 nm. I-CloisNa possessed a smooth, amorphous quartz silicon oxide structure (Fig. 1B) with an electron-dense, compacted appearance (Fig. 2). This differed from I-Clois30B's quartz silicon oxide structure which exhibited morphologies including smooth, pocketed, [16, 17] and platelet-like structures, although at significantly larger sizes than Clois30B. Incinerated particles showed comparable sizes (mean width ranging 1636 ± 98 to 1731 ± 108 nm) with DLS data comparing to FESEM data. Incinerated nanoclays showed comparable ρ_{EV} ranging 1.26 to 1.39. Dispersed CS had a fractured, crystal-like morphology and displayed single micron size with comparable ρENM and ρ_{EV} to incinerated nanoclays. DLS hydrodynamic diameter was 40% smaller than FESEM width measurements. Zeta potentials were slightly negative (− 6.8 to − 10.3) with minimal changes in pH across all tested particles. Lastly, all endotoxin levels in particle stock suspensions were below the kit's lower detection limit (Additional file 3: Table S4). Additional details on physicochemical characterization are presented in Supplemental Material.

Confirmation of THP-1 cell differentiation and T_H1 polarization

Differentiation of THP-1 cells into attached macrophages was confirmed with increased CD11b positive staining and lysosomes compared to THP-1 monocytes

Table 2 Particle characteristics of pre- and post-incinerated nanoclay in THP-1 cell culture medium

	CloisNa	Clois30B	I-CloisNa	I-Clois30B	CS
XRD analysis					
Basal spacing (nm)	1.21	1.85	Not present	Not present	n/a
Crystal structure	Montmorillonite; dioctahedral	Montmorillonite; dioctahedral	Amorphous quartz SiO_2	Quartz	Quartz
RPMI + 10% FBS					
SEM morphology	Single or small stacked platelets	Small or large stacked platelets	Smooth, amorphous	Amorphous; pocketed; platelet-like	Fractured, crystal-like
SEM mean length (nm)	379 ± 24	1270 ± 193	2872 ± 186	2392 ± 133	953 ± 36
SEM mean width (nm)	237 ± 15	857 ± 129	1731 ± 108	1636 ± 98	618 ± 24
Z average (nm)*	294.6 ± 3.1	205.7 ± 29.9	1795 ± 14.6	1495 ± 940	369.7 ± 7.51[a]
PdI*	0.388 ± .020	0.43 ± .035	0.417 ± .025	0.569 ± .077	0.535 ± .062
ζ*	− 10.3 ± .4	− 6.8 ± .3	− 9.8 ± .3	− 10.1 ± .4	− 9.0 ± .4
pH*	7.80 ± 0.02	7.82 ± 0.0	7.76 ± 0.07	7.83 ± 0.01	7.78 ± 0.01
Particle density ρENM (g/cm^3)	2.86	1.98	2.196[†]	2.65[†]	2.65
Mean effective density ρEV (g/cm^3)[b]	1.066 ± 0.001[A]	1.244 ± 0.018[B]	1.389 ± 0.020[DE]	1.264 ± 0.010[BC]	1.373 ± 0.018[DE]
THP-1 cellular uptake	Endosomes	Endosomes, some loss of intact endosome	Endosomes, acellular	Endosomes, acellular	Endosomes

SEM values represent means ± 1SE (n = 108–437)

*Values represent means ± 1SE of independent experiments (n = 3–6)

[a] Value did not agree with SEM measurements

[b] A theoretical stacking factor of 0.634 was used to calculate ρE

[A to E] Different capital letters indicate those ρEV significantly different from each other ($p < 0.05$)

[†] Not determined; estimated density based on XRD data and [105]

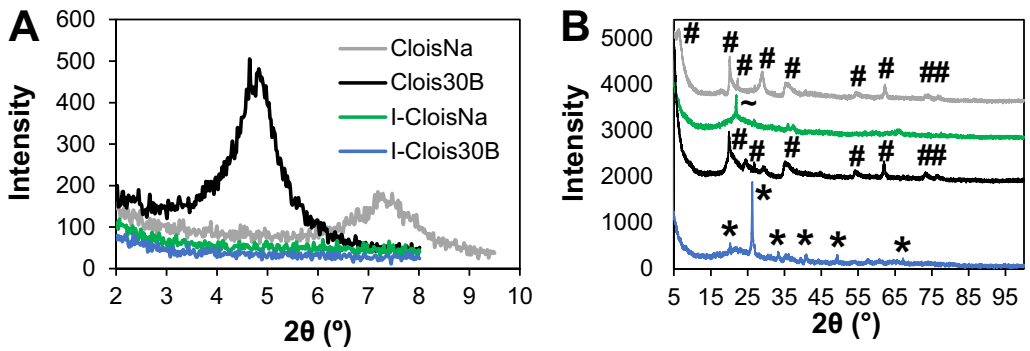

Fig. 1 Structure and dispersed particle size analyses of nanoclays **A** X-ray diffraction analysis of pristine and organomodified montmorillonite nanoclays (ONC) and their incinerated byproducts. Basal spacing of nanoclays in the 2–9.5° 2θ range indicated that ONC (Clois30B) possessed greater spacing between clay platelet structure than pristine (CloisNa) nanoclay, confirming presence of the organomodifier coating. Both incinerated particles showed no evidence of platelet spacing structure. **B** Diffraction patterns determined that both pre-incinerated nanoclays exhibited montmorillonite structure (#). Incinerated ONC possessed quartz crystal structure (*) while I-CloisNa exhibited amorphous silica structure (~)

(Additional file 1: S2A and B; see Supplementary Results). LPS stimulation of macrophages produced a T_H1 macrophage inflammatory response compared to naïve macrophages (M_o) evidenced by increased TNFα, CCL2, IL-1β, IL-6, and IL-8 (Additional file 1: Figure S2C).

TEM and enhanced darkfield analysis of particle cellular uptake

Following 24 h exposure, robust amounts of single and stacked platelets of CloisNa were found in endosomes of differentiated THP-1 cells (Fig. 3). CloisNa appeared

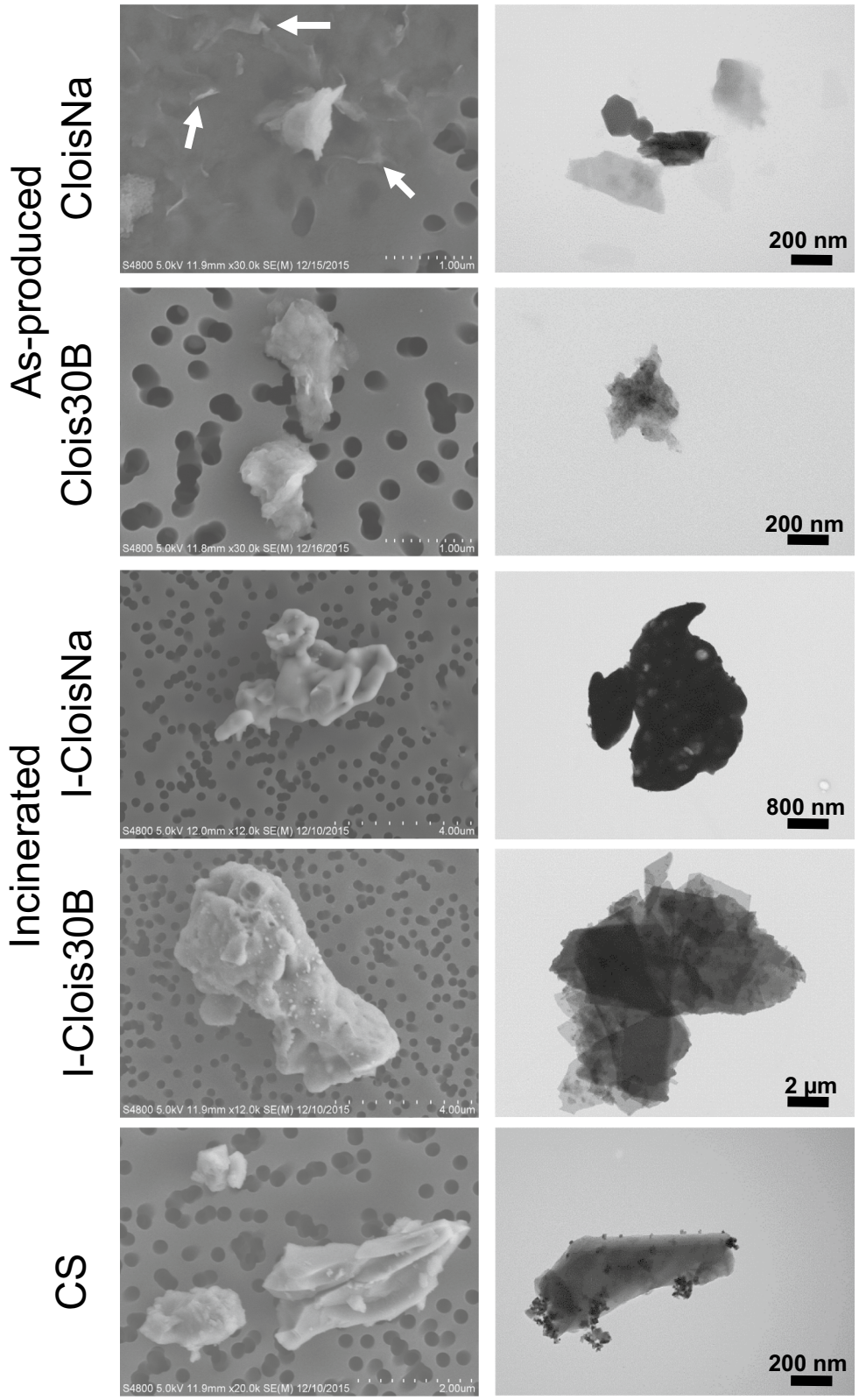

Fig. 2 Pre- and post-incinerated uncoated (CloisNa) and organomodified (Clois30B) montmorillonite nanoclay particle morphology under FESEM and TEM imaging. As-produced nanoclays possessed exfoliated (white arrows) and stacked platelet morphology while I-CloisNa showed amorphous pyrogenic silica morphology. I-Clois30B possessed a mixture of amorphous and retention of stacked platelet morphology, similar to crystalline silica (CS)

as a dense platelet shaped particles or as thin, dense platelets. To a lesser extent, Clois30B particles were also found in endosomes with instances of disappearance of an intact endosome membrane. Elemental mapping with TEM-EDS confirmed particle uptake in THP-1 cells (Additional file 1: Figures S3-7). Only smaller particle fractions (< 2 μm) of I-CloisNa and I-Clois30B were observed in THP-1 cell endosomes while larger single micron fractions were found in acellular areas or alongside THP-1 cells. Notably, I-CloisNa exposed THP-1 cells possessed large endosomes. CS was found within THP-1 cell endosomes indicating adequate uptake ability. These results paralleled those observed in BALF Cytospin samples at Day 1 post-aspiration exposure in C57BL/6J mice (Additional file 1: Figure S8). CloisNa, Clois30B, and CS particles were located within collected alveolar macrophages. Both incinerated nanoclays particles were found engulfed by a single macrophage or extracellularly associated with several macrophages. Collectively, this indicated that sub-micron, pre-incinerated nanoclay particles were more likely to undergo macrophage uptake, enclosed in endosomes, and interact with intracellular components.

Particle type-dependent differential THP-1 macrophage cytotoxicity and inflammatory response

Since all aspirated particles displayed a high propensity to interact with macrophages in in vivo exposures, we conducted quantitative HTS in vitro screening approaches to identify potential modes of action for macrophage cytotoxicity and inflammation responses in the absence and presence of LPS. Clois30B exposure caused significant decreased cell viability (4.8-fold) compared to all other particles with the largest maximal response (> 80% at highest dose; Clois30B $ED_{50} = 4.1$ μg/cm^2; all others $ED_{50} > 20$ μg/cm^2). Comparatively, all other nanoclays caused dose-dependent reductions in WST-1 at doses > 0.6 μg/cm^2 at 24 h. Clois30B exposure retained this potent cell viability reduction ability without LPS co-exposure (Clois30B $ED_{50} = 5.4$ μg/cm^2; Fig. 4A, Table 3). LPS-primed THP-1 cells were less sensitive to CloisNa-induced loss of cell viability compared to unprimed cells ($ED_{50} = 11.1$ μg/cm^2). These results were largely reflected in live cell imaging analysis (Fig. 4B; Additional file 1: Figure S9), though the threshold of cell viability loss was generally higher at > 0.6 μg/cm^2. Clois30B exposure caused significantly greater toxicity (3.2- to 4.7-fold) than both incinerated nanoclays and CS ($p \leq 0.02$), with a non-significant increase compared to CloisNa value ($p = 0.053$; Table 3; Additional file 1: Figure S10). Without LPS co-exposure CloisNa and Clois30B exposure resulted in significant loss of cell viability (58% and 87% at 20 μg/cm^2, respectively) compared to controls as measured by WST-1 metabolism and live cell imaging with minimal shift in induction threshold (Fig. 5A, B; Table 3). Only 20 μg/cm^2 CloisNa showed a significant 33% increase in cytotoxicity (i.e. LDH) while Clois30B exposure caused a robust, dose-dependent increase in cytotoxicity (≥ 2 μg/cm^2; Fig. 5C). Incinerated nanoclays and CS showed minimal effect.

Since some nanoclays produced acute loss of cell viability, we evaluated nanoclays for release of DAMPs as evidence of interaction of nanoclay with the cell membrane, which is the MIE in the lung fibrosis AOP. Clois30B exposure caused a dose-dependent increase in IL-1α and ATP, two well-established DAMPs, with significant levels at ≥ 0.6 μg/cm^2 (Fig. 5D, E) compared to unexposed cells. I-Clois30B and CS caused a significant moderate increase in IL-1α at 0.06 μg/cm^2 while only CloisNa caused a significant increase in ATP at 0.6 μg/cm^2. All other treatment groups showed no significant effect.

Next, CloisNa exposure caused a dose-dependent decrease (≥ 2 μg/cm^2) in THP-1 cell mitochondrial membrane potential (MMP) while all other particles had no effect when compared to unexposed cells. This effect was mirrored in a dose-dependent drop in intracellular ROS production in CloisNa-exposed cells (Fig. 5F, G). Notably, most CloisNa-exposed THP-1 cells were still observed on plates while Clois30B-exposed cells were clearly absent at high toxic doses with clear evidence of cell debris, potentially suggesting complete cell lysis or at least detachment of THP-1 cells at the time of measurement. Since engineered nanomaterial exposures are associated with apoptosis induction and/or inflammasome activation in vitro [53], treated THP-1 cells were assessed for markers of inflammasome activation resulting in pyroptotic cell death and apoptosis via caspase 3/7 activity. Analysis showed that CloisNa exposure induced a mixed pyroptotic and apoptotic profile, as determined by moderate significant increase in cathepsin

(See figure on next page.)

Fig. 3 Uptake and localization of pre- and post-incinerated uncoated (CloisNa) and organomodified (Clois30B) montmorillonite nanoclay in differentiated THP-1 macrophages in the absence of LPS. Cells were exposed to a 0.6 μg/cm^2 dose in 6-well plates for 24 h, followed by trypsinization, centrifugation, pellet fixation, sectioning, and imaging under TEM and TEM-STEM. Both bright and dark field detectors were used to collect images and EDS analyses. All nanoclay particles (white arrows) and crystalline silica were confirmed using EDS elemental analysis (n = 3; Additional file 1: Figures S3-7)

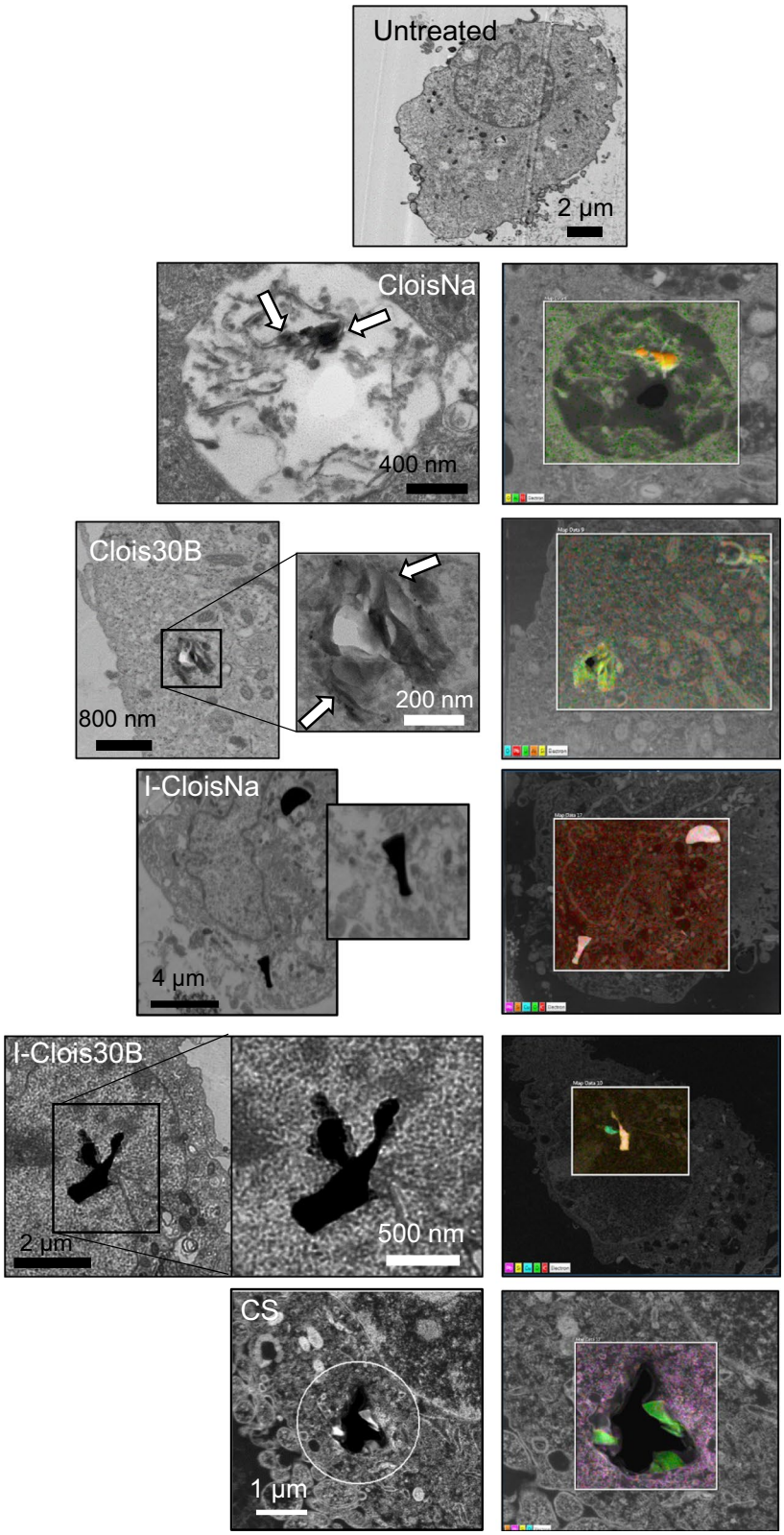

Fig. 3 (See legend on previous page.)

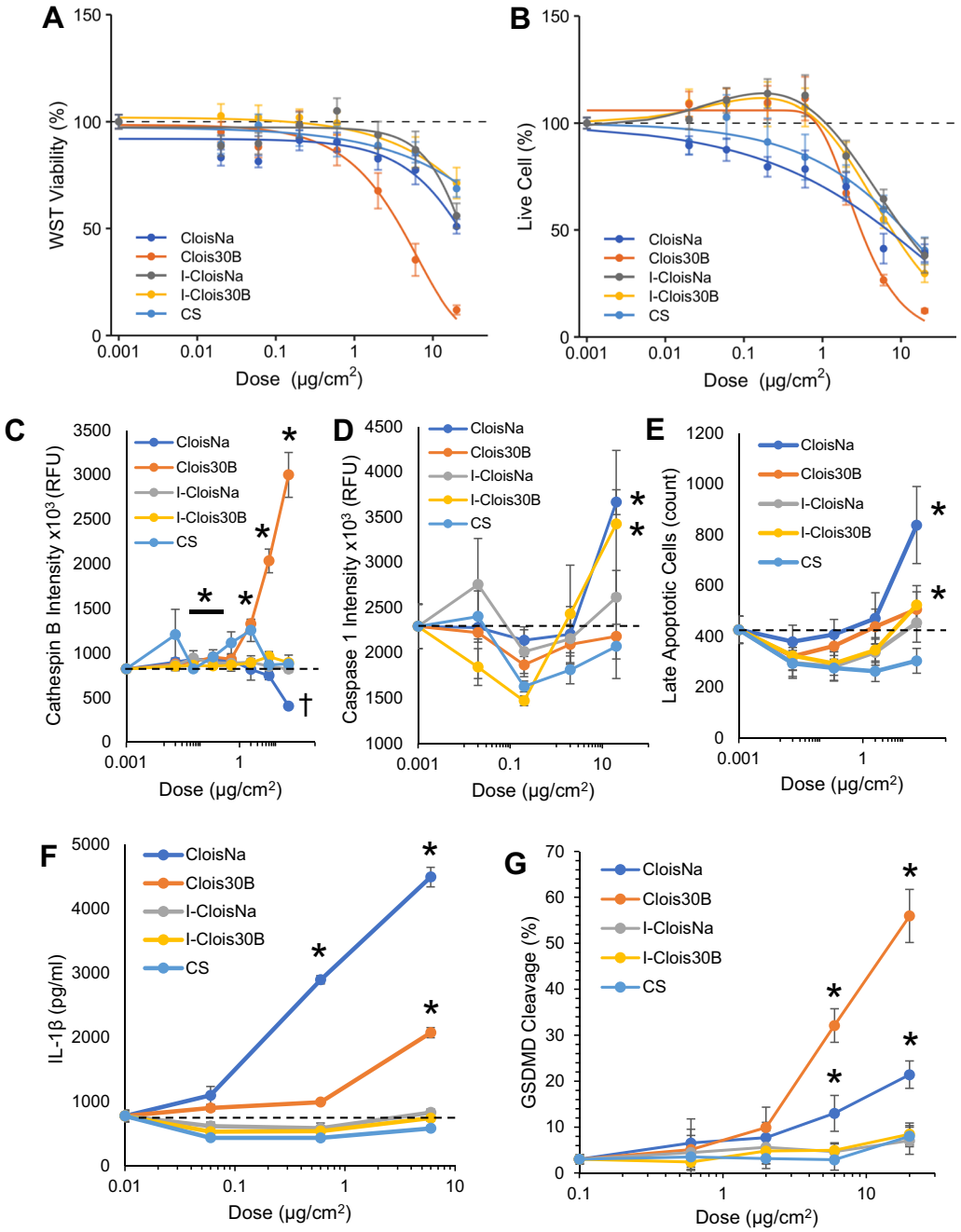

Fig. 4 Quantitative HTS toxicity data of differentiated THP-1 cells exposed to pre- and post-incinerated organomodified nanoclays in the presence of LPS. **A** Cell viability via WST-1 assay and B) live/dead counts at 24 h indicated that Clois30B produced a robust cytotoxic effect on THP-1 cells compared to all other particles. **C** Cathepsin B release, **D** Caspase 1, and **E** late apoptosis in exposed THP-1 cells at 6 h post-exposure **F** Secreted IL-1β levels from nanoclay-exposed THPs at 24 h. **G** Gasdermin D N-terminus (GSDMD) cleavage product indicating inflammasome-induced pyroptosis. All HTS measures reflect mean ± SE integrated intensities. Horizontal dotted line indicates unexposed control level. * and † indicates those treatments with a significant increase or decrease from unexposed cells, respectively ($p \leq 0.05$, n = 3–4)

B release (0.06 and 0.2 µg/cm^2), caspase 1 activity, markers of caspase 3/7 activity, and extracellular IL-1β release. Clois30B-treated THP-1 cells, by contrast, induced significant dose-dependent elevations in putative markers of the pyroptotic cell death pathway: Cathepsin B release, GSDMD-NT cleavage, and IL-1β release (Fig. 4C–G; Additional file 1: Figure S11). CloisNa exposure caused a significant, but intermediate increase in GSDMD-NT

Table 3 ED_{50} comparison (μg/cm^2) of pre- and post-incinerated nanoclay exposures to differentiated human THP-1 macrophages in the presence or absence of LPS

Assay	Particle	With LPS	Without LPS
WST-1	CloisNa	> 20*,a	11.1 ± 3.5
	Clois30B	4.1 ± 0.7	5.4 ± 2.0
	I-CloisNa	> 20*,a	> 20*,†,a
	I-Clois30B	> 20*,a	> 20*,†,a
	CS	> 20*, a	> 20*,†,a
Live cell imaging	CloisNa	6.8 ± 2.00	15.2 ± 6.9
	Clois30B	2.4 ± 0.5[b]	2.9 ± 0.6[b]
	I-CloisNa	11.1 ± 2.5*	> 20*,a
	I-Clois30B	7.6 ± 1.4*	> 20*,a
	CS	11.1 ± 03.5*	> 20*,a

* and †denote those particles with significantly different ED_{50} values from Clois30B and CloisNa, respectively ($p \leq 0.05$, n = 4 independent experiments)

[a] Estimated ED_{50} value was greater than the highest tested dose (20 μg/cm^2). Standard error of the mean values were not reported for these estimates

[b] Clois30B exhibited a non-significant lower ED_{50} than CloisNa with ($p = 0.053$) and without ($p = 0.062$) LPS

compared to untreated controls, while IL-1β levels were significantly higher than Clois30B-treated cells. Incinerated nanoclay analogues or CS did not cause acute pyroptotic or apoptotic cell death in LPS-stimulated THP-1 cells. Collectively, these findings suggest that differences in surface chemistry on pre-incinerated nanoclay impact mode of cell death in exposed macrophages.

Given the differences in THP-1 in vitro cell death mechanism and the differential inflammatory response in vivo, multiplex analysis of secreted or released in vitro cytokines and chemokines following acute nanoclay exposure (0–6 μg/cm^2) was conducted to evaluate differences in THP-1 cell inflammatory signaling, increased secretion of pro-inflammatory mediators (KE1), and their correlation to in vivo effect. Particle co-exposure with LPS produced a response dominated by IL-1β secretion with magnification of cytokine release at lower doses (Fig. 6A). IL-1β, IL-7, and IL-13, known key drivers of leukocyte recruitment, clustered together with their overexpression primarily associated with higher pre-incinerated nanoclay doses. Dose-dependent cytokine release following CloisNa and Clois30B exposures including those associated with acute inflammation (IL-1β, IL-7), IL-17α, T_H2 (IL-4, IL-13, eotaxin) and pro-fibrotic responses (PDGF-ββ, FGFβ; Additional file 3: Table S5). This large cluster of cytokines was more responsive to Clois30B than CloisNa at 0.06 μg/cm^2, showed minimal response to incinerated nanoclay exposure, and showed decreased secretion (20–25%) in response to CS exposure. LPS co-stimulation caused moderate doses of both nanoclays to elicit elevated acute damage (IL-6), T_H2 (IL-5, GM-CSF), and IL-15, while elevated IL-1ra was alone elevated following Clois30B exposure. Next, a group of cytokines (IP-10, MCP-1, IL-8, and IL-10) with decreased secretion (63–90%) was primarily associated with pre-incinerated nanoclays. Acute incinerated nanoclay and CS exposure produced minimal response compared to LPS-only exposed cells. Lastly, non-significant elevated IL-1ra levels were primarily associated with I-Clois30B and CS exposure. In a similar experiment of pre-incinerated nanoclays in the absence of LPS, an acute inflammatory response cytokine cluster (MIP1α, MIP1β, IFNγ, TNFα, and IL-8) displayed a different expression pattern across particle type compared to a large $T_H1/T_H2/T_H17$ cytokine cluster (Fig. 6B). CloisNa and Clois30B produced the most similar secreted mixed $T_H1/T_H2/T_H17$ cytokine profile with noticeable clustering of cytokines with similar functions. Dose-dependent significant increases in acute pro-inflammatory mediators (IL-1β, MIP1α, MIP1β), acute cell damage and T_H1 (IL6, IL-12p70), T_H2 and T_H17 allergic response (IL-4, IL-5, eotaxin, GM-CSF, IL-17α), STAT3 pathway-associated T cell regulation (IL-2 and IL-15), and wound healing/pro-fibrotic (FGFβ, PDGF-ββ) signals were observed (Additional file 3: Table S6). Significant 1.3- to 7.1-fold increases occurred with IFNγ, TNFα, VEGF, IL-7, and IL-10, while decreases in RANTES and IP-10 were only observed with increasing doses of CloisNa. Conversely, the incinerated nanoclay exposure produced a comparatively muted response and possessed strikingly different profiles than pre-incinerated forms, with I-CloisNa clearly the most acutely inflammatory. Only the 6 μg/cm^2 dose of both incinerated nanoclays produced noticeable similar acute inflammatory versus $T_H1/T_H2/T_H17$ cytokine clusters. Notably, both IL-5 and IL-6 were secreted across all doses of I-CloisNa. I-CloisNa was also

(See figure on next page.)

Fig. 5 Differentiated THP-1 macrophage cell metabolism, DAMP release, mitochondrial membrane potential, and ROS at 24 h post-exposure in the absence of LPS. **A** CloisNa and Clois30B exposure both reduced THP-1 cell WST-1 metabolic activity. **B** CloisNa and Clois30B exposure caused a dose-dependent decrease in live cell counts while **C** Clois30B exposure caused a dose-dependent increase in cytotoxicity (LDH). **D**, **E** Clois30B produced dose-dependent release of DAMPs (IL-1α and ATP) while all other particles had significant minimal or no effect. **F** Only CloisNa caused a dose-dependent mitochondrial membrane depolarization. **G** Intracellular reactive oxygen species using CellROX. Points represent mean ± SE. Horizontal dashed bar represents unexposed cell level. * and † indicated significant increase and decrease compared to unexposed cells, respectively ($p \leq 0.05$, n = 4)

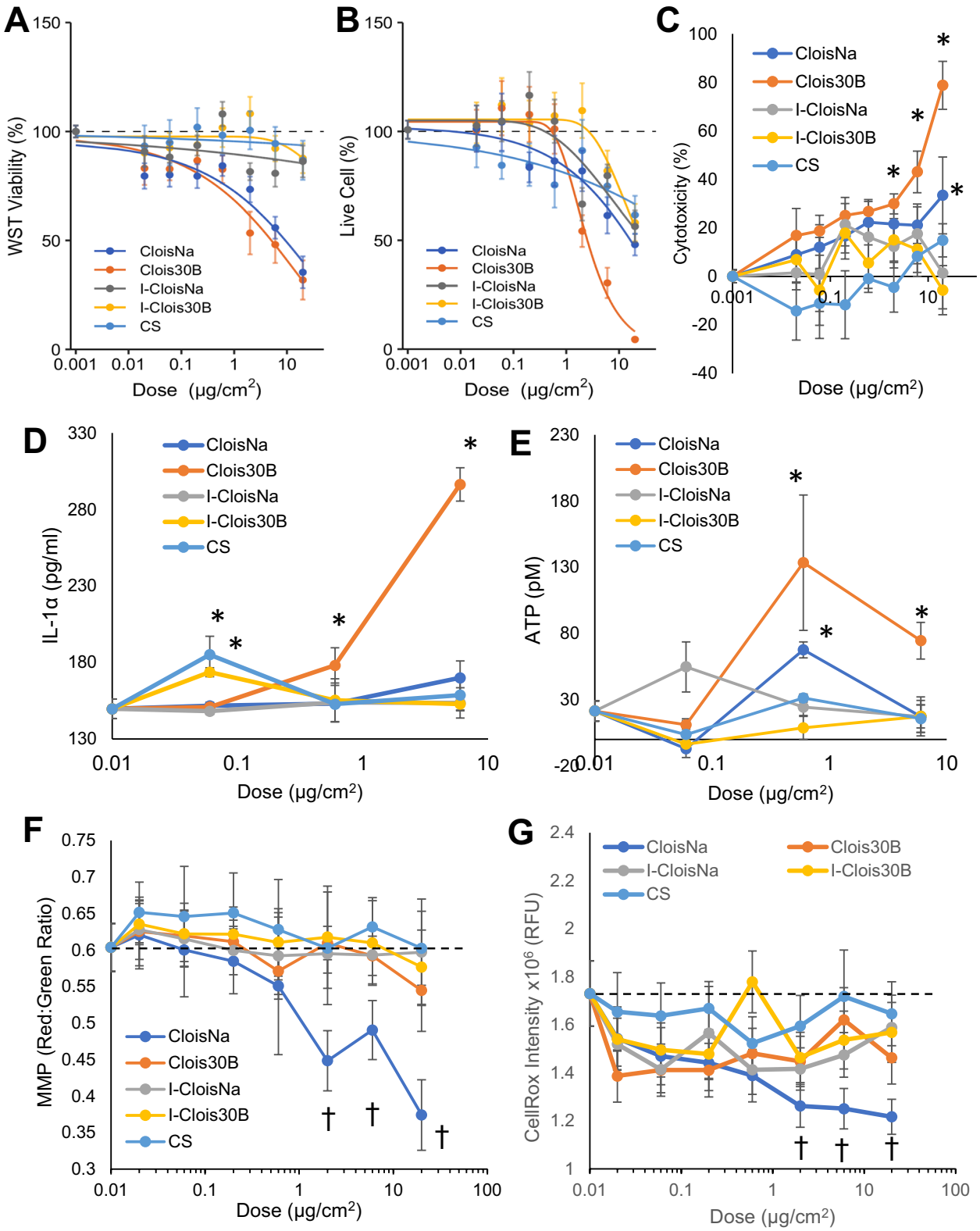

Fig. 5 (See legend on previous page.)

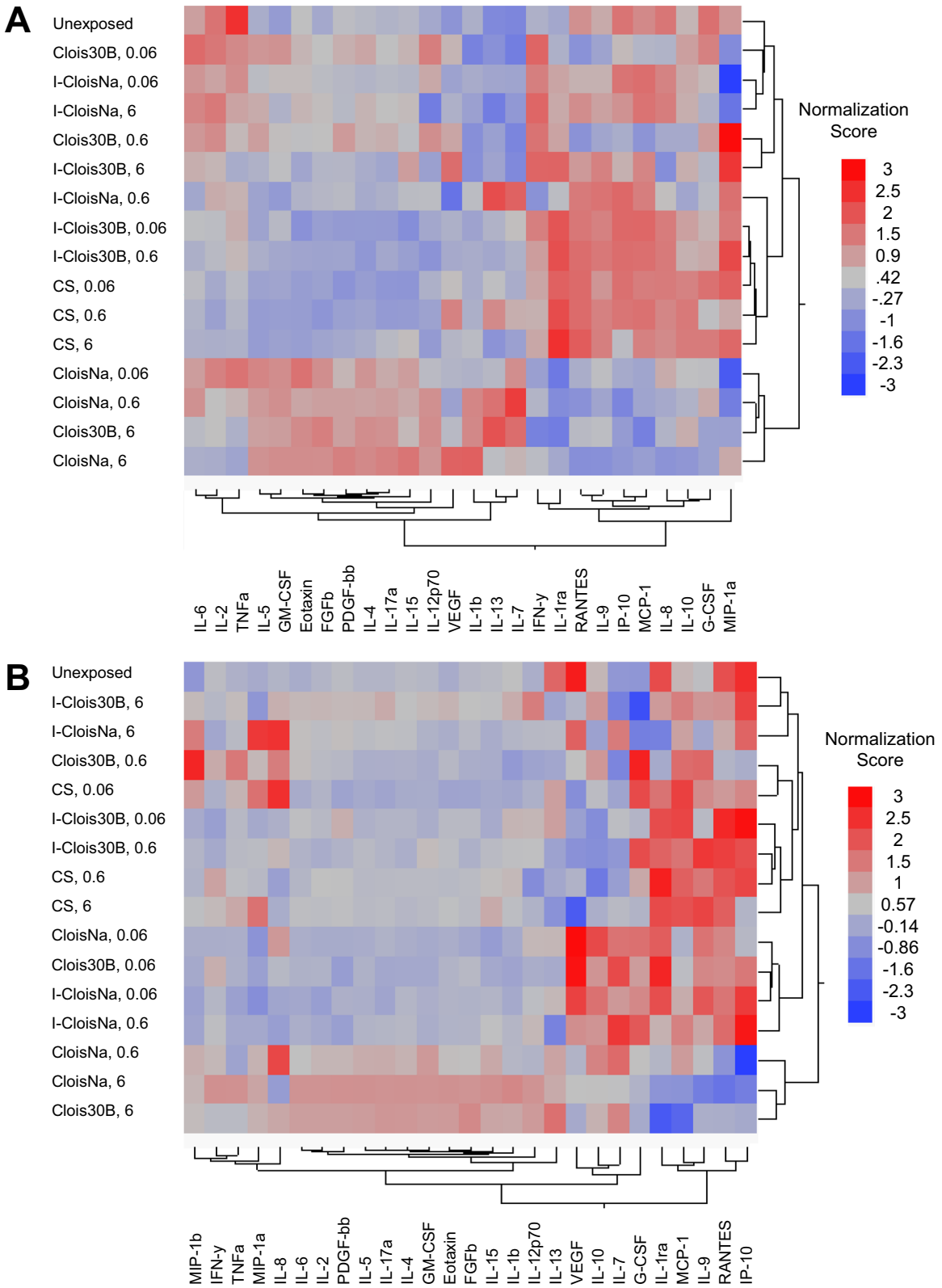

Fig. 6 Secreted cytokine response profile of differentiated THP-1 macrophage cells following pre- and post-incinerated nanoclay exposure for 24 h (n = 3). **A** Cells exposed to particles in the presence of LPS. Pre-incinerated nanoclay exposure caused an inflammatory profile which differed from post-incinerated nanoclays and crystalline silica (CS). **B** Cells exposed to particles in the absence of LPS

more acutely inflammogenic (e.g., TNFα, IL-6, IL-1β, IL-5) than CS, though both dampened VEGF secretion. CS exposure produced a minimal response with increased MIP-1β and non-significant increase in MIP1α. A summary of differentiated THP-1 cell response to pre- and post-incinerated nanoclays is presented in Table 4.

In vitro THP-1 macrophage response correlation to in vivo BAL inflammatory indices

In vitro to in vivo comparison analyses across all tested particles found that WST-1 and live cell count response in a tenfold in vitro dose scheme (0.6 and 6 μg/cm^2) above the equivalent in vivo dose (30 and 300 μg/lung) produced significant moderate correlations with in vivo BAL total cell, monocyte, and lymphocyte counts in Day 7 post-exposure animals, regardless of LPS presence in THP-1 cultures (Fig. 7; Additional file 3: Table S7). In addition, non-LPS THP-1 cell LDH release at equivalent in vitro doses (0.06 and 0.6 μg/cm^2) significantly correlated with in vivo BAL total cell and neutrophils on Day 1 and 7, and with monocytes and leukocytes on Day 7. Correlation of non-LPS THP-1 cell viability to Day 1 BAL cell differential endpoints was not significant, except for neutrophils at tenfold dose equivalent. Notably, the addition of LPS co-stimulation lowered the in vitro dose range for in vivo correlation with significant correlation of live cell count occurring with neutrophils. Both CloisNa and Clois30B treatments showed the strongest reliance on this trend. Next, gasdermin D cleavage and IL-1β levels, but not Cathepsin B release, in THP-1 in vitro model strongly correlated with in vivo BAL total cell, monocyte, neutrophil, and lymphocyte counts at Day 7 (Additional file 1: Figure S12, Additional file 3: Table S8). Notably, in vitro IL-1 β levels correlated with Day 1 BAL total cell and monocyte counts, with LPS co-stimulated cells showing a moderate to strong correlation at equivalent mass doses. Cathepsin B release strongly correlated with Day 28 BAL total cell, monocyte, and lymphocyte data most likely due to the low response profile at this late point.

Table 4 Summary of THP-1 macrophage acute toxicity and inflammation response to pre- and post-incinerated organomodified nanoclay exposure in the presence or absence of LPS

Endpoint	Clois Na	Clois 30B	I-CloisNa	I-Clois30B	CS
Crystal structure	Montmorillonite	Montmorillonite	Amorphous quartz	Crystalline quartz	Crystalline quartz
Mean particle size in RPMI (μm)	0.304	1.064	2.302	2.104	0.786
Cellular uptake	+++; endosome	++; endosome	+; endosome	+; endosome	ND
w LPS					
WST-1 viability[a]	> 20	4.11	> 20	> 20	> 20
Live cell count[a]	6.82	2.36	11.06	7.56	11.06
LDH cytotoxicity (%)	n/a	n/a	n/a	n/a	n/a
Cathepsin B	**1.1**	**2.47**	1.05	1.17	1.05
Caspase I	**1.60**	− 1.05	1.14	**1.49**	− 1.11
Late apoptosis	**1.97**	1.19	1.07	**1.23**	− 1.41
IL-1β	**5.80**	**2.67**	1.07	− 1.04	− 1.33
Gasdermin D cleavage (%)	**13.00**	**32.11**	4.62	4.93	2.89
Inflammatory profile	IL-1β, $T_H1/T_H2/T_H17$	IL-1β, $T_H1/T_H2/T_H17$	Minimal	IL-1ra	IL-1ra
w/o LPS					
WST-1 viability[a]	11.13	5.41	> 20	> 20	> 20
Live cell count[a]	15.32	2.91	> 20	> 20	> 20
LDH cytotoxicity (%)	14.5	**74.6**	22.5	16.4	13.6
IL-1α	1.14	**1.97**	1.06	**1.16**	**1.24**
ATP	**3.19**	**6.2**	2.56	− 6.0	1.46
MMP	**-1.23**	− 1.02	− 1.02	1.01	1.05
Reactive oxygen species	− 1.39	− 1.06	− 1.18	− 1.12	− 1.01
Inflammatory profile	$T_H1/T_H2/T_H17$	$T_H1/T_H2/T_H17$	$T_H1/T_H2/T_H17$	MIP-1β, TNFα, IL-2, Eotaxin, FGFβ	MIP-1β

All data represent mean fold change compared to unexposed cells unless otherwise noted

[a] Calculated EC_{50} values (μg/cm^2)

+++ high; ++ moderate; + modest. *ND* not determined. *n/a* not applicable

Bold font indicates a significant difference compared to unexposed controls

n = 3–4 independent experiments

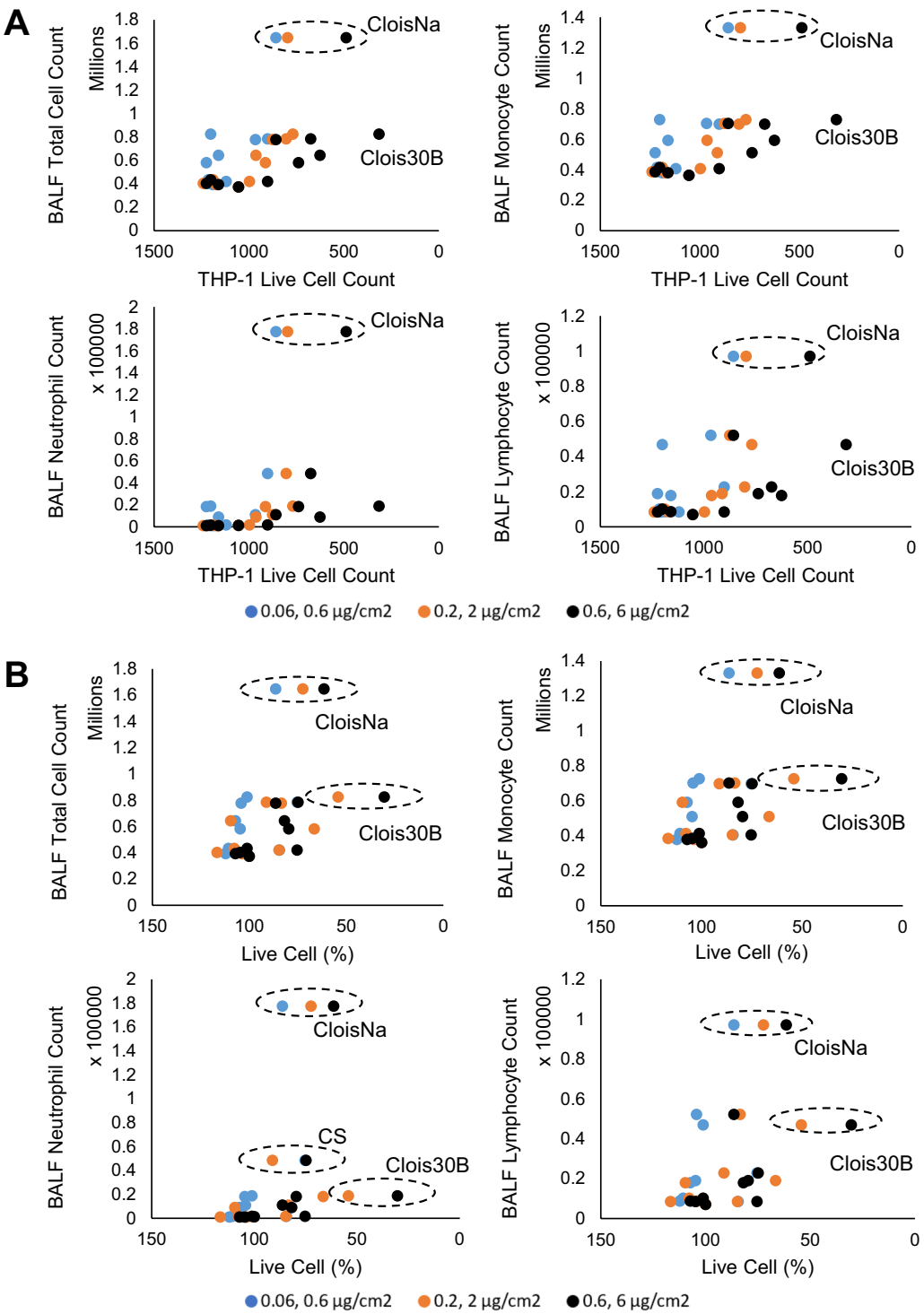

Fig. 7 Representative plots of **A** LPS and **B** non-LPS stimulated THP-1 macrophage cell viability metrics significantly correlated to BAL cell differentials at Day 7 post-exposure following pre- and post-incinerated nanoclay particle exposure. Data from all particle types are presented. Most significant correlations were found with THP-1 live cell count in LPS stimulated cells (**A**) and non-LPS stimulated cells (**B**; Additional file 3: Table S7). Decreases in live THP-1 macrophages correlated with increased BAL immune cell counts. Comparisons were made at three different in vitro dose equivalent ratios (blue 0.06 and 0.6 µg/cm^2; orange 0.2 and 2 µg/cm^2; black 0.6 and 6 µg/cm^2) versus in vivo aspiration doses (30 and 300 µg /lung) in male C57Bl/6J mice. Particle names and hashed ovals call out noticeable differences between CloisNa, Clois30B, and CS responses

Next, Clois30B in vitro 24 h exposure at 0.6 μg/cm^2 to non-LPS stimulated THP-1 macrophages produced a cytokine response significantly correlated with the equivalent 300 μg/lung response in Day 1 exposed mouse lung (Fig. 8A; Table 5). MIP-1α, MIP-1β, TNFα, and IL-8/MIP2 were the cytokines most responsive to both models for Clois30B, thus indicating their potential role as inflammatory markers in future ONC toxicology studies. I-CloisNa at 6 μg/cm^2 animals showed significant positive correlations with 300 μg/lung at Day 1 post-exposure (Fig. 8B). MIP-1α, MIP-1β, and IL-8/MIP2 showed elevated levels in both models. All other particles showed no significant correlation relationships between models or particle treatments did not elicit significant THP-1 cell cytokine production. Co-stimulation with LPS showed no significant correlation of in vitro versus in vivo pro-inflammatory cytokine response (Additional file 3: Table S9).

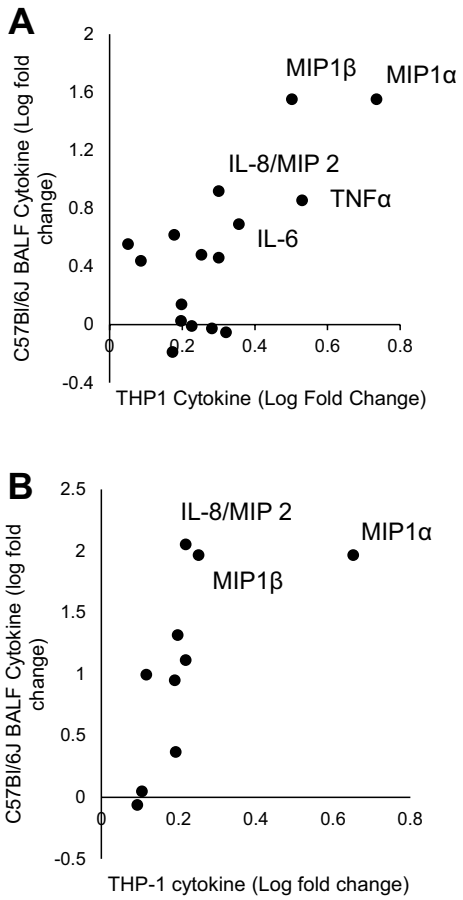

Fig. 8 Representative plots of significant in vitro macrophage/in vivo BAL inflammatory cytokine correlation. **A** THP-1 cell cytokine profile after 24 h Clois30B 0.6 μg/cm^2 exposure correlation with 300 μg Day 1 post-exposure BAL cytokine inflammatory profile in male C57Bl/6J mice. **B** I-CloisNa 6 μg/cm^2-exposed THP-1 profile correlation with 300 μg Day 1 BAL profile in male C57Bl/6J mice. All other comparison correlations were not significant

Table 5 Correlation coefficients of equivalent dose non-LPS stimulated THP-1 cells versus C57Bl/6J BALF (300 μg) at Day 1 and 7 post-exposure for 16 pro-inflammatory cytokines

	CloisNa	Clois30B	I-CloisNa	I-Clois30B	CS
24 h 0.6 μg/cm^2 versus Day 1 300 μg/lung					
r	0.16	**0.69**	n/a	n/a	n/a
p value	0.56	**0.003***	–	–	–
24 h 6 μg/cm^2 versus Day 1 300 μg/lung					
r	− 0.07	0.33	**0.88**[a]	n/a	n/a
p value	0.81	0.22	**0.001**	–	–
24 h 0.6 μg/cm^2 versus Day 7 300 μg/lung					
r	0.33	0.44	n/a	n/a	n/a
p value	0.21	0.08	–	–	–
24 h 6 μg/cm^2 versus Day 7 300 μg/lung					
r	− 0.15[a]	0.01[a]	0.38[a]	n/a	n/a
p value	0.58	0.97	0.14	–	–

* Indicates those log-transformed correlations that were statistically significant ($p \leq 0.05$)

[a] Non-parametric data; Spearman's coefficient correlation analysis was performed

n/a indicates correlations not performed due to treatments producing minimal statistically significant THP1 cytokines

Correlation analyses for each cytokine between the two models for nanoclay particles revealed that equivalent in vitro dose 0.6 μg/cm^2 at 24 h versus in vivo 300 μg/lung Day 1 post-exposure resulted in no significant correlations. Increasing the in vitro dose tenfold (6 μg/cm^2) showed significant strong positive correlation with in vivo Day 1 for IL-6, Eotaxin, PDGF-ββ, and IL-12p70 (Additional file 3: Table S10). Macrophages exposed to 0.6 μg/cm^2 for 24 h showed significant, strong positive correlations to 300 μg/lung Day 7 post-exposure for IL-1β, IL-10, and PDGF-ββ. Strong positive correlations (non-significant) also existed for IL-6 and eotaxin ($p \leq 0.06$). Most of these significant correlations were driven by increased cytokine expression from both pre-incinerated nanoclays with minimal responses from incinerated nanoclays or CS. In summary, among all particle types, in vitro macrophage loss of cell viability, gasdermin D cleavage, IL-1β release, and a select number of cytokines correlated with in vivo BAL inflammation responses.

Discussion

The HTS in vitro screening and protein secretion profiling studies support the hypothesis that physicochemical characteristics, namely surface coating and incineration status, of nanoclays along their life cycle influence inflammation and cytotoxic effects in human macrophages. In

addition, these findings correlated with previous in vivo inflammatory responses, thus identifying macrophage as a key cell type that modulate adverse effects following pre- and post-incinerated nanoclay particle exposure. These findings match the molecular initiating event (substance interaction with lung cell membrane components) and first key events (KE1 increased pro-inflammatory mediators, KE2 increased inflammatory cell recruitment) in the proposed lung fibrosis AOP #173 [37]. A summary of this study's findings with and without LPS stimulus is presented in Fig. 9. Lastly, the findings suggest that in vitro model using human alveolar macrophage can serve as a potential screening tool for acute nanoclay in vivo exposure-induced lung toxicity.

Using both non- and LPS co-exposure assisted in identifying key factors driving macrophage response to nanoclay exposure. Other particle studies including metals, silica, and PM2.5 report that LPS, alarmins (e.g. TNFα, IL-1α), and exogenous pathogen molecular patterns act to prime the macrophage inflammasome to produce a IL-1β and IL-18 inflammatory response [28, 54, 55]. LPS priming allowed us to identify underlying mechanisms driving inflammatory response. By using non-LPS exposed macrophages, we identified nanoclay exposure-induced release of DAMPs, altered mitochondrial polarization, and improved correlations with our in vivo study's inflammatory response findings.

Pre-incinerated nanoclays were more acutely toxic to macrophages compared to post-incinerated nanoclay and CS particles matching findings previously reported [16, 19]. However, dose–response curves among particles differed based on the assay indicating potential differences in mode of toxic action due to the presence/absence of a QAC coating. CloisNa exposure (i.e. no organic coating) resulted in uptake of nanoclay particles in endosomes, caused decreased cell viability, and moderate cell membrane damage (i.e. LDH release) indicating the cell death mechanism was potentially more dependent on internal cell death mechanism, and less than plasma membrane lysis. Alternatively, Clois30B exposure reduced THP-1 cell viability which coincided with LDH and DAMP (i.e. IL-1α, and ATP) release suggesting that plasma membrane damage is a potential mode of action for ONC-induced macrophage toxicity, which aligns with previous studies [56, 57] and confirms the MIE in the lung fibrosis AOP [37].

Our results indicate that moderate CloisNa exposure aligns with a NLRP3 inflammasome-mediated macrophage pyroptosis which involves endocytosed particle damaging phagolysosome membranes, increasing permeability, releasing proteolytic enzymes (e.g. Cathespin B), thereby initiating the NLRP3 inflammasome, Caspase 1 cleavage [17], gasdermin D cleavage [58], and IL-1β release [27]. The observed release of ATP into conditioned medium also potentially acted as an inflammasome activation signal through $P2X_7$ receptor resulting in K^+ ion efflux [58], a known rate limiting step inflammasome activation. Silica, carbon nanotubes, and titanium nanobelts were shown to induce lysosome membrane permeability and downstream cathepsin B activation of NLRP3 inflammasome [59]. Silica nanoparticles induce the NLRP3/Caspase-1/GSDMD pathway in cardiomyocytes in both in vivo and in vitro inhalation exposure models. Large graphene oxide, a 2-D nanoparticle, exposure to Kupffer cells cause lipid peroxidation following phagocytosis, calcium flux, mitochondrial ROS generation, and NLRP3/Caspase-1/GSDMND-mediated pyroptosis [54, 55]. Here, higher doses of CloisNa, however, caused MMP loss which coincided with apoptosis/necrosis and cell viability dose–response curves. Cathepsin B release is known to regulate Bcl2 degradation, thus increasing Bax/Bak pore formation in the outer mitochondrial membrane, mitochondrial depolarization, and subsequent apoptosis [60–62]. Damaged mitochondria can occur following particle-induced phagolysosome leakage (e.g. carbon black nanoparticles) or direct particle damage (e.g. residual fly ash, nano-ZnO) to mitochondria which enhances NLRP3 inflammasome formation [63–67]. Mitochondrial depolarization has been described as a decision point for apoptotic signaling [68]. Past studies with nanosilica and quartz particulate exposure reported loss of MMP, increased mitochondrial ROS production, and increased apoptosis [69, 70]. Elevated intracellular ROS appears to not play a role in THP-1 cell inflammatory or cytotoxicity responses following pre-incinerated nanoclay exposure and matches previously reported in vitro and in vivo findings [15, 17, 19, 57, 71]. This mode of action is well-established for other silicates and aluminosilicates [14] and contributes to their pro-inflammatory effect.

Clois30B particle uptake without an intact endosome membrane in surviving macrophages suggests potential membrane damage or passive uptake of these particle with a hydrophobic coating. Previous studies hypothesized that dissolution of the QAC coating into physiological fluids or in vitro cell culture medium is the initiating event for ONC exposure-induced toxicity [15, 22, 72]. Solubilization of QAC coating from Clois30B was previously observed in cell culture medium suspensions [23, 72]. Cationic lipids, such as QACs, can interact with lipid membranes resulting in endosome disruption, ROS production, and cell necrosis [73]. However, filtration studies reported that a wide diversity of nanoclay with QAC coatings exhibited more cytotoxic potency than solubilized coating [22, 25]. For THP-1 cells, this suggests that exposure to particle-bound QAC, both extra- and

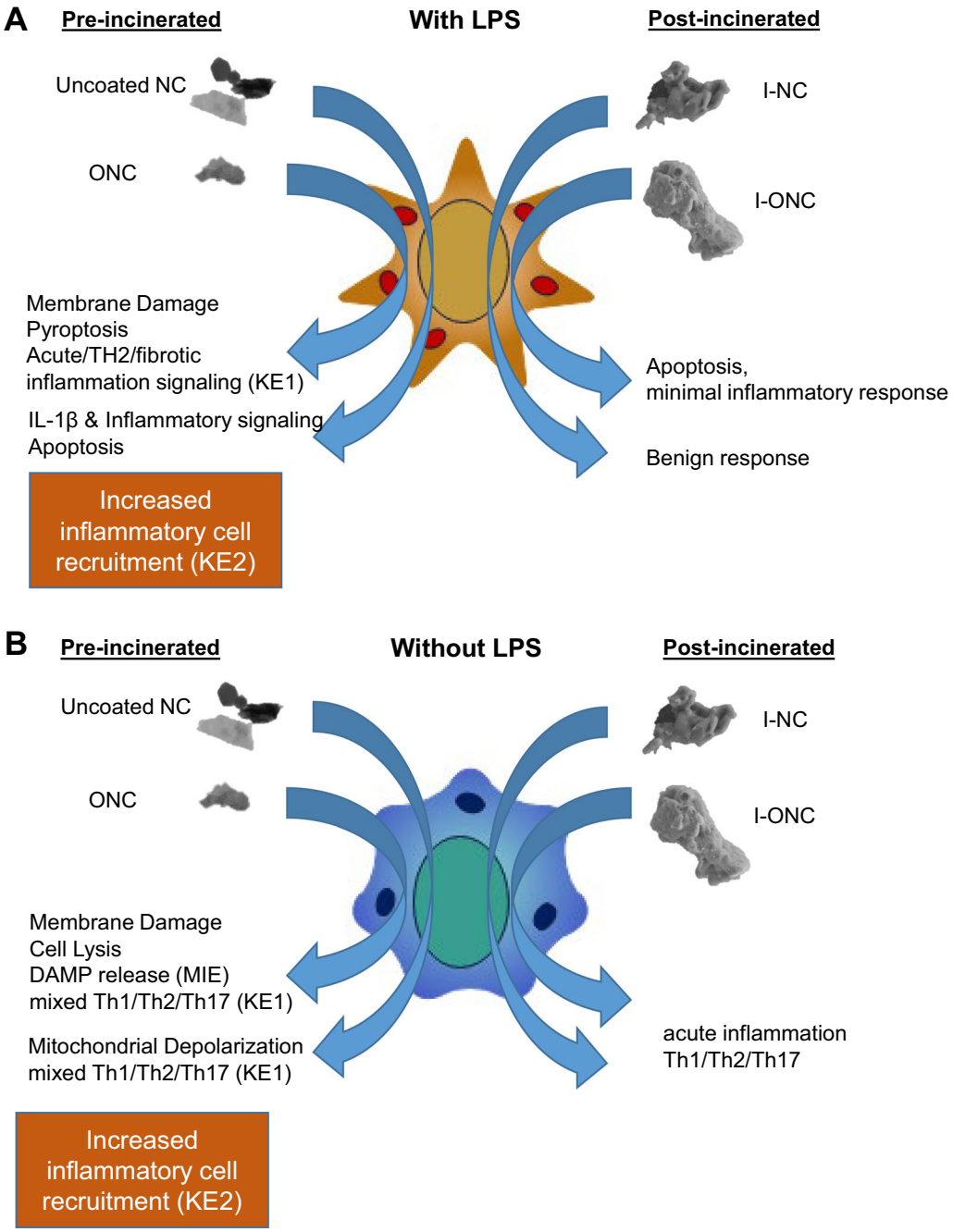

Fig. 9 Proposed airway macrophage response to pre- and post-incinerated nanoclay particles in the **A** presence or **B** absence of lipid polysaccharide and its role in pulmonary fibrosis AOP. With LPS co-stimulation, uncoated nanoclay (NC) exposure caused a robust inflammatory response (KE1) and apoptosis while ONC exposure caused membrane damage, pyroptosis, and an acute T_H2 inflammation (KE1) signal. Incinerated nanoclay exposure resulted in apoptosis, minimal inflammatory (I-ONC), or a relatively benign (I-NC) response. In a sterile exposure model uncoated NC and ONC exposure caused DAMP release (MIE), mitochondrial membrane depolarization and cell lysis, respectively, along with a mixed $T_H1/T_H2/T_H17$ pro-inflammatory response (KE1). Incinerated nanoclay exposure collectively produced an acute mixed $T_H1/T_H2/T_H17$ inflammatory response. These findings for pre-incinerated nanoclays aligned with increased inflammatory cell recruitment in the in vivo model (KE2)

intracellularly, potentially disrupts both cellular plasma and endosome membranes causing robust DAMP release (i.e. IL-1a and ATP), rapid induction of the NLRP3 inflammasome and pyroptosis/necrosis, prior to cleavage of pro-IL-1β taking place. In our in vivo model, both CloisNa and Clois30B induced Caspase 1 cleavage in

whole lung lysate at Day 7 post-exposure [17]. In THP-1 cells, higher doses of Clois30B did not elicit a strong IL-1β release, but dose-dependent response curves from cell viability, cell metabolism, membrane damage, and IL-1α release trended well with cathepsin B release and Gasdermin D cleavage suggesting a pyroptotic mode of action. Liu et al. showed that cleaved GSDMD-NT binds to cellular membranes to form pores causing membrane permeability, leading to cell lysis and IL-1β release [51]. In this study, the lack of strong Caspase 1 activity, especially for Clois30B, suggests LPS activation of other caspases, such as non-canonical caspases or Caspase 8, may cleave Gasdermin D to initiate nanoclay-induced pyroptosis [34, 74]. Alternatively, necrotic macrophages release the master alarmin IL-1α which leads to elevated IL-1β secretion in surviving macrophages [75]. The inherent absence of apoptosis contradicts some previous ONC in vitro findings [15], but aligns with several studies in that methyl dihydroxylethyl hydrogenated tallow ammonium and other QAC coatings on nanoclay have minimal apoptotic induction ability [18, 22, 57]. Several different occupational inhalation hazards are known to induce acute lung damage and low initial or delayed inflammation response including Cd/Se-ZnS quantum dots, in part due to slow dissolution rates [76]. Low IL-1β release, but with enhanced IL-1α, ATP, TNFα, IL-6, and IL-8 release at high ONC doses suggests that pyroptosis and necrosis occurs quickly and releases alarmins upon macrophage breakdown [77], but cells are not intact to undergo proper inflammasome-mediated IL-1β release [60, 78]. Alternatively, it has been shown that autophagy may disrupt IL-1β release by targeting ubiquitinated inflammasomes [79]. Low IL-1β release may also partially explain the low and delayed inflammatory response observed in lung tissue in vivo. Slow solubilization of the QAC coating from Clois30B most likely induced a delayed response in vivo resulting in enhanced moderate inflammatory profile with alarmins and low IL-1β at Day 7 [17].

Human THP-1 macrophage release of mixed T_H1/T_H2/T_H17 cytokines following pre-incinerated nanoclay exposure and uptake supports the KE1 secretion of pro-inflammatory cytokines in the lung fibrosis AOP. This matches the in vivo response that included nanoclay uptake by macrophages, mixed T_H1/T_H2/T_H17 inflammatory and pro-fibrotic cytokine profile, and monocyte recruitment following nanoclay deposition in the terminal bronchiole and surrounding alveoli [17]. Silica, aluminum, aluminosilicates, and asbestos are well known to cause acute damage to airway and alveoli [14] with a well-established T_H1 and T_H17 inflammatory response [80–82]. Similar acute inflammatory response with elevated IL-1α, IL-1β, TNFα, IL-6, and IL-8 were recently reported in a 3D alveolar model following both nanosilica and crystalline silica [83] and in THP-1 cells following nanosilica exposure [84]. The T_H2 response (IL-4, IL-5, eotaxin, IL-17α) participates in regulating and maintaining homeostasis during acute phase inflammatory response [85], assists in wound repair of lung lesions [86, 87], and facilitate these particles to act as sensitization adjuvants [88]. This may be a more important factor for ONCs that possess a QAC organic coating since many QACs are known to induce an allergic sensitization response following inhalation or dermal exposure [89, 90]; however, this area requires further research. Interestingly, elevated levels of several T cell chemotaxis, differentiation, and proliferation signals (IL-2, IL-15, IL-7, IL-9) were observed which may partially explain elevated lymphocyte levels at Day 7 following in vivo exposure [17]. However, the role of T cell types, levels, and involvement of T cell-mediated immunological responses during silica pathogenesis [80] are not fully elucidated in nanoclay toxicology and remain a potential area for future research.

Enhanced in vitro secretion of IL-6, GM-CSF, MIP1α/β, MIP-2, and TNFα in exposed THP-1 cells matched in vivo model response at Day 7 and 28 post-exposure. Macrophages typically secrete these factors following silica particulate exposure and play roles in development of adverse lung pathology. For example, prolonged elevated levels of MIP1α and MCP-1 promote chronic lung fibrotic disease [91] while IL-6 is an important driver of bleomycin-induced lung fibrosis in mice [92]. GM-CSF is typically secreted by macrophages, epithelial cells, and fibroblasts in the lung following silica particulate exposure and promotes eosinophil recruitment and stimulates fibroblast collagen production [93, 94]. Collectively, these findings suggest that macrophage exposure to pre-incinerated nanoclay promotes monocyte, eosinophil, and fibroblast chemotaxis and activation that persists in vivo, indicating elevated pro-fibrotic signaling. In both of our in vitro and in vivo models, however, a distinction between how the presence and absence of the organomodifier coating influences inflammation profile and mode of cytotoxicity was clear. Pristine nanoclay (CloisNa) exposure elicited increased TNFα, IFNγ, and IL-10 secretion suggesting an enhanced macrophage chemotaxis and granuloma formation ability compared to Clois30B. Notably, Clois30B only induced TNFα and VEGF secretion in vivo and not in vitro suggesting that another cell type, such as dendritic cells, lymphocytes, or PMNs may secrete these cytokine sources and enhance T_H1 in vivo response as suggested by previous studies [27, 91, 95, 96].

Comparatively, incineration drastically changed nanoclay particle structure with complete degradation of platelet crystal structure, increased particle

size/reduced surface area, and complete loss of the QAC modifier [16] which lead to minimal to moderate reductions in THP-1 live cell counts, apoptosis, and inflammatory potential, with LPS co-exposure increasing sensitivity to cytotoxicity and cell death. The observed morphological and crystal structural differences between I-CloisNa and I-Clois30B moderately impacted cellular responses. The absence of an organic coating allowed for cooling silica oxide to form an amorphous quartz silicon oxide (i.e. I-CloisNa) [97] while presence of the organic coating allowed for some maintenance of a quartz structure (i.e. I-Clois30B) which follows previous findings [98, 99]. Following in vivo exposure, large incinerated particulate with surrounding macrophage was observed in lung tissue while small endocytosed particulate was observed both in tissue and BALF cytospins [17]. Amorphous silica, such as I-CloisNa, possesses high inflammatory potential that is transient in nature with little persistent effect [14, 17]. I-CloisNa clearly displayed elevated inflammatory ability over I-Clois30B at equal high dose in non-LPS stimulated THP-1 cells with elevated levels of TNFα, IL-1β, IL-5, IL-17α, IL-15 and PDGF-ββ which matched in vivo acute transient BALF inflammatory response, increased Caspase 1 cleavage, NF-κB, and Nrf2 expression in lung tissue [17]. I-Clois30B's mixed morphology of amorphous and platelet-like silica [16, 18] produced a similar inflammatory cytokine profile compared to I-CloisNa, with both highly differing from CS. Interestingly, our finding that I-Clois30B crystal structure matches that of quartz further explains the increase in chronic inflammation in the in vivo model in concordance with the BALF cytokine profile and histopathology of CS-exposed animals. Crystalline silica was previously shown to cause acute mild inflammation and perturb macrophage phagocytosis and apoptosis that results in chronic inflammation and elevated risk of silicosis [14, 100]. The absence of CS effect following acute exposure is possibly due to the absence of reactive silanol groups on aged CS [14] and the retention of some amorphous silica particles within the I-Clois30B sample [16, 17]. Recent increased research into nano-sized, surface coatings, vitreous, and sub-micron amorphous silica largely supports that amorphous surfaces can elicit acute inflammatory responses, but may exhibit reduced toxicity compared to uncoated, crystalline, or highly reactive surface chemistries [14, 101, 102]. The morphological and toxicodynamic similarities of I-Clois30B and CS, in the absence of the QAC coating, indicate the crystalline structure becomes the prevailing factor dictating chronic inflammatory response. This is juxtaposed to I-CloisNa with a pyrogenic amorphous structure and acute, but transient, inflammatory effect. This indicates that prolonged incinerated ONC exposure represents a potential risk to long-term pulmonary health.

In vitro to in vivo correlation analyses revealed that in vitro model for human alveolar macrophage for cell viability, IL-1β release, and gasdermin D cleavage moderately to strongly aligned with in vivo BAL monocyte, neutrophil, and lymphocyte cell infiltrate counts on either Day 1 or Day 7 post-exposure. Furthermore, it supports the role of macrophages in the KE1 release of pro-inflammatory mediators driving KE2 increased recruitment of pro-inflammatory cells in the proposed lung fibrosis AOP. Some of the stronger correlations occurred with 3- or 10-fold increase in in vitro dose above the in vivo equivalent mass per area dose. This is not surprising since in vivo mass dose assumes that particles deposit entirely in the respiratory bronchi/alveoli and homogeneously across the alveolar surface in the lung while assuming macrophages are not mobile. Since macrophages are mobile with a primary function to remove foreign material, it is expected that intracellular mass dose will be well above the local deposited mass dose. Next, non-LPS exposed macrophage cytokine profiles correlated with in vivo BAL profile (while LPS-stimulated macrophages did not) as both in vitro and in vivo hazard characterization studies are conducted in pathogen-free conditions with sterile particles. This analysis identified a five-cytokine profile (MIP1α, MIP1β, IL-8, TNFα, IL-6) for ONC that could be used in future nanoclay in vitro toxicity studies to screen for inflammatory effects. A previous ONC study also found in vitro macrophage IL-8 expression correlated with their in vivo findings [26]. Lastly, several cytokines involved in T_H2 cell recruitment and fibrosis (IL-6, eotaxin, PDGF-ββ, IL-10, IL-1β) were released from macrophages in vitro and correlated with in vivo BAL response, which aligns with KE4 (T_H2 cell activation) in the lung fibrosis AOP. Collectively, this suggests in vitro macrophage response assessment as an appropriate in vitro screening tool for ONC lung toxicology research.

Given the diversity of different morphologies and chemistries along nanoclay life cycles, traditional in vivo toxicity testing is not feasible. Here, we used a tiered screening strategy evaluating relationships between particle physicochemical properties and biological effect. Limitations to the study include uncertainty in deposited dose based on differences in effective density and heterogeneity in particle suspensions and how in vitro doses relate to unknown in vivo deposited doses in the deep lung following known administered dose. Improvements to this approach can be developed to rapidly identify those nanoclays that pose elevated risk in occupational

settings during handling and disposal processes [50, 103, 104].

Conclusions

Herein, we evaluated two types of montmorillonite nanoclay and their incinerated byproducts for their toxicological and immunological profiles. We found clear evidence that physicochemical differences, namely presence/absence of QAC coating and incineration status, of nanoclays determines key events and molecular signaling patterns associated with lung macrophage inflammatory and cytotoxic responses. Further, we found correlations between toxicological and immunological effects observed in vitro to those observed in a mouse model, adding to our understanding of ONC's toxic mechanism along its life cycle and demonstrating the suitability of the in vitro non-LPS primed differentiated THP-1 model as a screening tool for nanoclays along their lifecycle.

Abbreviations

AOP	Adverse outcome pathway
CloisNa	Cloisite® Na, uncoated montmorillonite
Clois30B	Cloisite® 30B, organomodified montmorillonite
I-CloisNa	Incinerated Cloisite® Na^+
I-Clois30B	Incinerated Cloisite® 30B
CS	Heat-inactivated crystalline silica
DLS	Dynamic light scattering
ELISA	Enzyme-linked immunosorbent assay
FESEM	Field emission scanning electron microscopy
GSDMD	Gasdermin D
GSDMD-NT	Gasdermin D N-terminus
HTS	High-throughput screening
LDH	Lactate dehydrogenase
LPS	Lipopolysaccharide
MMP	Mitochondrial membrane potential
ONC	Organomodified nanoclay
PdI	Particle dispersity index
QAC	Quaternary ammonium compound
RPMI	Roswell Park Memorial Institute
TEM	Transmission electron microscopy
THP-1	Human monocytic cells
WST-1	Water soluble tetrazolium salt—1
XRD	X-ray diffraction

Supplementary Information

The online version contains supplementary material available at https://doi.org/10.1186/s12989-024-00577-7.

Additional file 1: Figures. 1–12 documenting particle characterization, uptake, high-throughput imaging, and protein expression data.

Additional file 2: Methods for fluorescent high content imaging of macrophage differentiation, differentiation results, and detailed physicochemical analysis results.

Additional file 3: Tables x S1–10 containing particle characterization, secreted cytokine levels, and correlation coefficients.

Acknowledgements

We thank the WVU Shared Research Facility and WVU Analytical Lab for their assistance with this study.

Author contributions

TAS acquired funding, designed, carried out the study, and wrote the manuscript. JJ and JC designed and performed automated imaging studies and analyses. RD, TGK, and LR provided technical support, assisted animal work, and writing of manuscript. SF and AD performed electron microscopy sample preparation and analysis. SA and RG provided nanoclay advice and assisted in drafting the manuscript. AW and CZD conducted XRD analysis and assisted in drafting manuscript.

Funding

This study was supported by grants from the NIOSH Nanotechnology Research Center (939051L and 921043S), National Science Foundation Grant Nos. 1434503 and 1454230, the National Institutes of Health (ES022968), and a grant from the King Abdulaziz City for Science and Technology (Riyadh, Saudi Arabia).

Availability of data and materials

A majority of the data generated or analyzed during this study are included in this published article [and its Supplemental information files]. Additional datasets used during the current study and the code block for generating ED_{50} curves are available from the corresponding author on reasonable request or can be found on the NIOSH Data and Statistics Gateway.

Declarations

Ethics approval

The animal study protocol and procedures were approved by the NIOSH IACUC.

Consent for publication

Not applicable.

Competing interests

The authors declare that they have no competing interests. The findings and conclusions in this article are those of the author(s) and do not necessarily represent the official position of the National Institute for Occupational Safety and Health, Centers for Disease Control and Prevention. Mention of product names does not constitute endorsement.

Author details

[1]Health Effects Laboratory Division, National Institute for Occupational Safety and Health, 1095 Willowdale Road, Morgantown, WV 26505, USA. [2]Chemical and Biomedical Engineering, West Virginia University, Morgantown, WV 26506, USA.

Received: 14 July 2023 Accepted: 8 March 2024
Published online: 21 March 2024

References

1. Research TM. Nanoclay (kaolinite, smectite, and others) market for packaging, flame retardants, automotive, paints & coatings, and other end-users- global industry analysis, size, share, growth, trends and forecast 2015–2023. 2015.
2. Alateyah A, Dhakal H, Zhang ZJ. Processing, properties, and applications of polymer nanocomposites based on layer silicates: a review. Adv Polym Technol. 2013;32(4).
3. Patel HA, Somani RS, Bajaj HC, Jasra RV. Nanoclays for polymer nanocomposites, paints, inks, greases and cosmetics formulations, drug delivery vehicle and waste water treatment. Bull Mater Sci. 2006;29(2):133–45.
4. Huang Y, Zhang M, Zou H, Li X, Xing M, Fang X, He J. Genetic damage and lipid peroxidation in workers occupationally exposed to organic bentonite particles. Mutat Res Genet Toxicol Environ Mutagen. 2013;751(1):40–4.
5. Zeng SLYZY, Zhang QF, Du YJ, Sun YT, Zhang MJ. Study on occupational standard of bentonite dust in air of workplace. Chin J Ind Hyg Occup Dis. 1998;16:177–8.

6. Mackevica A, Foss HS. Release of nanomaterials from solid nanocomposites and consumer exposure assessment—a forward-looking review. Nanotoxicology. 2016;10(6):641–53.
7. Tsai CS-J, White D, Rodriguez H, Munoz CE, Huang C-Y, Tsai C-J, et al. Exposure assessment and engineering control strategies for airborne nanoparticles: an application to emissions from nanocomposite compounding processes. J Nanopart Res. 2012;14(7):989.
8. Tsai S, Ashter A, Ada E, Mead JL, Barry CF, Ellenbecker MJJAAQR. Airborne nanoparticle release associated with the compounding of nanocomposites using nanoalumina as fillers. Aerosol Air Qual Res. 2008;8(2):160–77.
9. Froggett SJ, Clancy SF, Boverhof DR, Canady RA. A review and perspective of existing research on the release of nanomaterials from solid nanocomposites. Part Fibre Toxicol. 2014;11:17.
10. Pourchez J, Chivas-Joly C, Longuet C, Leclerc L, Sarry G, Lopez-Cuesta JM. End-of-life incineration of nanocomposites: new insights into nanofiller partitioning into by-products and biological outcomes of airborne emission and residual ash. Environ Sci Nano. 2018;5(8):1951–64.
11. Floody MC, Theng B, Reyes P, Mora MJCM. Natural nanoclays: applications and future trends–a Chilean perspective. Clay Miner. 2009;44(2):161–76.
12. Lopes AC, Martins P, Lanceros-Mendez S. Aluminosilicate and aluminosilicate based polymer composites: present status, applications and future trends. Prog Surf Sci. 2014;89(3):239–77.
13. Adamis Z, Williams RB. Bentonite, kaolin and selected clay minerals. 1st ed. Geneva: World Health Organization; 2005.
14. Pavan C, Fubini B. Unveiling the variability of "quartz hazard" in light of recent toxicological findings. Chem Res Toxicol. 2017;30(1):469–85.
15. Maisanaba S, Pichardo S, Puerto M, Gutierrez-Praena D, Camean AM, Jos A. Toxicological evaluation of clay minerals and derived nanocomposites: a review. Environ Res. 2015;138:233–54.
16. Wagner A, Eldawud R, White A, Agarwal S, Stueckle TA, Sierros KA, et al. Toxicity evaluations of nanoclays and thermally degraded byproducts through spectroscopical and microscopical approaches. Biochim Biophys Acta Gen Subj. 2017;1861(1 Pt A):3406–15.
17. Stueckle TA, Davidson DC, Derk R, Kornberg TG, Battelli L, Friend S, et al. Short-term pulmonary toxicity assessment of pre- and post-incinerated organomodified nanoclay in mice. ACS Nano. 2018;12(3):2292–310.
18. Stueckle TA, White A, Wagner A, Gupta RK, Rojanasakul Y, Dinu CZ. Impacts of organomodified nanoclays and their incinerated byproducts on bronchial cell monolayer integrity. Chem Res Toxicol. 2019;32(12):2445–58.
19. Wagner A, White AP, Stueckle TA, Banerjee D, Sierros KA, Rojanasakul Y, et al. Early assessment and correlations of nanoclay's toxicity to their physical and chemical properties. ACS Appl Mater Interfaces. 2017;9(37):32323–35.
20. Wagner A, White AP, Tang MC, Agarwal S, Stueckle TA, Rojanasakul Y, et al. Incineration of Nanoclay Composites Leads to Byproducts with Reduced Cellular Reactivity. Sci Rep. 2018;8(1):10709.
21. Maisanaba S, Hercog K, Filipic M, Jos A, Zegura B. Genotoxic potential of montmorillonite clay mineral and alteration in the expression of genes involved in toxicity mechanisms in the human hepatoma cell line HepG2. J Hazard Mater. 2016;304:425–33.
22. Janer G, Fernandez-Rosas E, Mas del Molino E, Gonzalez-Galvez D, Vilar G, Lopez-Iglesias C, et al. In vitro toxicity of functionalised nanoclays is mainly driven by the presence of organic modifiers. Nanotoxicology. 2014;8(3):279–94.
23. Sharma AK, Mortensen A, Schmidt B, Frandsen H, Hadrup N, Larsen EH, Binderup ML. In-vivo study of genotoxic and inflammatory effects of the organo-modified Montmorillonite Cloisite(R) 30B. Mutat Res Genet Toxicol Environ Mutagen. 2014;770:66–71.
24. Porter DW, Barger M, Robinson VA, Leonard SS, Landsittel D, Castranova V. Comparison of low doses of aged and freshly fractured silica on pulmonary inflammation and damage in the rat. Toxicology. 2002;175(1–3):63–71.
25. Di Ianni E, Møller P, Mortensen A, Szarek J, Clausen PA, Saber AT, et al. Organomodified nanoclays induce less inflammation, acute phase response, and genotoxicity than pristine nanoclays in mice lungs. Nanotoxicology. 2020;14(7):869–92.
26. Di Ianni E, Møller P, Vogel UB, Jacobsen NR. Pro-inflammatory response and genotoxicity caused by clay and graphene nanomaterials in A549 and THP-1 cells. Mutat Res Genet Toxicol Environ Mutagen. 2021;872:503405.
27. Pollard KM. Silica, silicosis, and autoimmunity. Front Immunol. 2016;7:97.
28. Sayan M, Mossman BT. The NLRP3 inflammasome in pathogenic particle and fibre-associated lung inflammation and diseases. Part Fibre Toxicol. 2016;13(1):51.
29. Villeneuve DL, Crump D, Garcia-Reyero N, Hecker M, Hutchinson TH, LaLone CA, et al. Adverse outcome pathway (AOP) development I: strategies and principles. Toxicol Sci. 2014;142(2):312–20.
30. Chang X, Tan YM, Allen DG, Bell S, Brown PC, Browning L, et al. IVIVE: Facilitating the use of in vitro toxicity data in risk assessment and decision making. Toxics. 2022;10(5):232.
31. McLean P, Mueller W, Gosens I, Cassee FR, Rothen-Rutishauser B, Boyles M, Tran L. Establishing relationships between particle-induced in vitro and in vivo inflammation endpoints to better extrapolate between in vitro markers and in vivo fibrosis. Part Fibre Toxicol. 2023;20(1):5.
32. Di Ianni E, Jacobsen NR, Vogel U, Møller P. Predicting nanomaterials pulmonary toxicity in animals by cell culture models: Achievements and perspectives. Wiley Interdisc Rev Nanomed Nanobiotechnol. 2022;14(6):e1794.
33. Mohd Yasin ZN, Mohd Idrus FN, Hoe CH, Yvonne-Tee GB. Macrophage polarization in THP-1 cell line and primary monocytes: a systematic review. Differentiation. 2022;128:67–82.
34. Lu F, Lan Z, Xin Z, He C, Guo Z, Xia X, Hu T. Emerging insights into molecular mechanisms underlying pyroptosis and functions of inflammasomes in diseases. J Cell Physiol. 2020;235(4):3207–21.
35. Shang Y, Sun Q. Particulate air pollution: major research methods and applications in animal models. Environ Dis. 2018;3(3):57–62.
36. Degobbi C, Saldiva PHN, Rogers C. Endotoxin as modifier of particulate matter toxicity: a review of the literature. Aerobiologia. 2011;27:97–105.
37. Halappanavar S SM, Wallin H, Vogel U, Sullivan K, Clippinger AJ. AOP 173: Substance interaction with the lung resident cell membrane components leading to lung fibrosis 2023. https://aopwiki.org/aops/173.
38. Castranova V, Dalal NS, Vallyathan V. Role of surface free radicals in the pathogenicity of silica. Silica and silicainduced diseases. Boca Raton: CRC Press. 1996. pp. 91–105
39. Cohen JM, Beltran-Huarac J, Pyrgiotakis G, Demokritou P. Effective delivery of sonication energy to fast settling and agglomerating nanomaterial suspensions for cellular studies: Implications for stability, particle kinetics, dosimetry and toxicity. NanoImpact. 2018;10:81–6.
40. Coyle JPDR, Kornberg TG, Singh D, Jensen J, Friend S, Mercer R, Stueckle TA, Demokritou P, Rojanasakul Y, Rojanasakul LW. Carbon nanotube filler enhances incinerated thermoplastics-induced cytotoxicity and metabolic disruption in vitro. Part Fibre Toxicol. 2020;17:1–21.
41. DeLoid G, Cohen JM, Darrah T, Derk R, Rojanasakul L, Pyrgiotakis G, et al. Estimating the effective density of engineered nanomaterials for in vitro dosimetry. Nat Commun. 2014;5:3514.
42. Yue Y, Kan Y, Choi H, Clearfield A, Liang HJAPL. Correlating hydrodynamic radii with that of two-dimensional nanoparticles. Appl Phys Lett. 2015;107(25):253103.
43. Xia T, Hamilton RF, Bonner JC, Crandall ED, Elder A, Fazlollahi F, et al. Interlaboratory evaluation of in vitro cytotoxicity and inflammatory responses to engineered nanomaterials: the NIEHS Nano GO Consortium. Environ Health Perspect. 2013;121(6):683–90.
44. Park EK, Jung HS, Yang HI, Yoo MC, Kim C, Kim KS. Optimized THP-1 differentiation is required for the detection of responses to weak stimuli. Inflamm Res. 2007;56(1):45–50.
45. Stueckle TA, Davidson DC, Derk R, Kornberg TG, Schwegler-Berry D, Pirela SV, et al. Evaluation of tumorigenic potential of CeO_2 and Fe_2O_3 engineered nanoparticles by a human cell in vitro screening model. NanoImpact. 2017;6:39–54.
46. Hubbs A, Greskevitch M, Kuempel E, Suarez F, Toraason M. Abrasive blasting agents: designing studies to evaluate relative risk. J Toxicol Environ Health A. 2005;68(11–12):999–1016.
47. Stone KC, Mercer RR, Freeman BA, Chang LY, Crapo JD. Distribution of lung cell numbers and volumes between alveolar and nonalveolar tissue. Am Rev Respir Dis. 1992;146(2):454–6.
48. Chambers KM, Mandavilli BS, Dolman NJ, Janes MS. General staining and segmentation procedures for high content imaging and analysis. Methods Mol Biol (Clifton, NJ). 2018;1683:21–31.

49. Mandavilli BS, Aggeler RJ, Chambers KM. Tools to Measure Cell Health and Cytotoxicity Using High Content Imaging and Analysis. Methods in molecular biology (Clifton, NJ). 2018;1683:33–46.
50. George S, Xia T, Rallo R, Zhao Y, Ji Z, Lin S, et al. Use of a high-throughput screening approach coupled with in vivo zebrafish embryo screening to develop hazard ranking for engineered nanomaterials. ACS Nano. 2011;5(3):1805–17.
51. Liu X, Zhang Z, Ruan J, Pan Y, Magupalli VG, Wu H, Lieberman J. Inflammasome-activated gasdermin D causes pyroptosis by forming membrane pores. Nature. 2016;535(7610):153–8.
52. Ritz C, Streibig JCJJSS. Bioassay analysis using R. J Stat Softw. 2005;12(5):1–22.
53. Nel A, Xia T, Meng H, Wang X, Lin S, Ji Z, Zhang H. Nanomaterial toxicity testing in the 21st century: use of a predictive toxicological approach and high-throughput screening. Acc Chem Res. 2013;46(3):607–21.
54. Daniels AU, Barnes FH, Charlebois SJ, Smith RA. Macrophage cytokine response to particles and lipopolysaccharide in vitro. J Biomed Mater Res. 2000;49(4):469–78.
55. Jämsen E, Pajarinen J, Kouri VP, Rahikkala A, Goodman SB, Manninen M, et al. Tumor necrosis factor primes and metal particles activate the NLRP3 inflammasome in human primary macrophages. Acta Biomater. 2020;108:347–57.
56. Geh S, Yücel R, Duffin R, Albrecht C, Borm PJ, Armbruster L, et al. Cellular uptake and cytotoxic potential of respirable bentonite particles with different quartz contents and chemical modifications in human lung fibroblasts. Arch Toxicol. 2006;80(2):98–106.
57. Lordan S, Higginbotham CL. Effect of serum concentration on the cytotoxicity of clay particles. Cell Biol Int. 2012;36(1):57–61.
58. Swanson KV, Deng M, Ting JP. The NLRP3 inflammasome: molecular activation and regulation to therapeutics. Nat Rev Immunol. 2019;19(8):477–89.
59. Jessop F, Hamilton RF Jr, Rhoderick JF, Fletcher P, Holian A. Phagolysosome acidification is required for silica and engineered nanoparticle-induced lysosome membrane permeabilization and resultant NLRP3 inflammasome activity. Toxicol Appl Pharmacol. 2017;318:58–68.
60. Katsnelson MA, Lozada-Soto KM, Russo HM, Miller BA, Dubyak GR. NLRP3 inflammasome signaling is activated by low-level lysosome disruption but inhibited by extensive lysosome disruption: roles for K^+ efflux and Ca^{2+} influx. Am J Physiol Cell Physiol. 2016;311(1):C83-c100.
61. Joshi GN, Knecht DA. Silica phagocytosis causes apoptosis and necrosis by different temporal and molecular pathways in alveolar macrophages. Apoptosis. 2013;18(3):271–85.
62. Xie Z, Zhao M, Yan C, Kong W, Lan F, Narengaowa, et al. Cathepsin B in programmed cell death machinery: mechanisms of execution and regulatory pathways. Cell Death Disease. 2023;14(4):255.
63. Yuan X, Nie W, He Z, Yang J, Shao B, Ma X, et al. Carbon black nanoparticles induce cell necrosis through lysosomal membrane permeabilization and cause subsequent inflammatory response. Theranostics. 2020;10(10):4589–605.
64. Caceres L, Abogunloko T, Malchow S, Ehret F, Merz J, Li X, et al. Molecular mechanisms underlying NLRP3 inflammasome activation and IL-1β production in air pollution fine particulate matter (PM(2.5))-primed macrophages. Environ Pollut (Barking, Essex: 1987). 2024;341:122997.
65. Kelley N, Jeltema D, Duan Y, He Y. The NLRP3 inflammasome: an overview of mechanisms of activation and regulation. Int J Mol Sci. 2019;20(13):3328.
66. Liu Q, Zhang D, Hu D, Zhou X, Zhou Y. The role of mitochondria in NLRP3 inflammasome activation. Mol Immunol. 2018;103:115–24.
67. Zhuo LB, Liu YM, Jiang Y, Yan Z. Zinc oxide nanoparticles induce acute lung injury via oxidative stress-mediated mitochondrial damage and NLRP3 inflammasome activation: In vitro and in vivo studies. Environ Pollut (Barking, Essex: 1987). 2024;341:122950.
68. Zamzami N, Marchetti P, Castedo M, Zanin C, Vayssiere J-L, Petit PX, Kroemer G. Reduction in mitochondrial potential constitutes an early irreversible step of programmed lymphocyte death in vivo. J Exp Med. 1991;181(5):1661–72.
69. Deville S, Honrath B, Tran QTD, Fejer G, Lambrichts I, Nelissen I, et al. Time-resolved characterization of the mechanisms of toxicity induced by silica and amino-modified polystyrene on alveolar-like macrophages. Arch Toxicol. 2020;94(1):173–86.
70. Wilhelmi V, Fischer U, van Berlo D, Schulze-Osthoff K, Schins RP, Albrecht C. Evaluation of apoptosis induced by nanoparticles and fine particles in RAW 264.7 macrophages: facts and artefacts. Toxicol In Vitro. 2012;26(2):323–34.
71. Maisanaba S, Puerto M, Pichardo S, Jorda M, Moreno FJ, Aucejo S, Jos A. In vitro toxicological assessment of clays for their use in food packaging applications. Food Chem Toxicol. 2013;57:266–75.
72. Sharma AK, Schmidt B, Frandsen H, Jacobsen NR, Larsen EH, Binderup ML. Genotoxicity of unmodified and organo-modified montmorillonite. Mutat Res. 2010;700(1–2):18–25.
73. Simberg D, Weisman S, Talmon Y, Barenholz Y. DOTAP (and other cationic lipids): chemistry, biophysics, and transfection. Crit Rev Ther Drug Carrier Syst. 2004;21(4):257–317.
74. Gram AM, Booty LM, Bryant CE. Chopping GSDMD: caspase-8 has joined the team of pyroptosis-mediating caspases. EMBO J. 2019;38(10):e102065.
75. Rabolli V, Badissi AA, Devosse R, Uwambayinema F, Yakoub Y, Palmai-Pallag M, et al. The alarmin IL-1α is a master cytokine in acute lung inflammation induced by silica micro- and nanoparticles. Part Fibre Toxicol. 2014;11:69.
76. Roberts JR, Antonini JM, Porter DW, Chapman RS, Scabilloni JF, Young S-H, et al. Lung toxicity and biodistribution of Cd/Se-ZnS quantum dots with different surface functional groups after pulmonary exposure in rats. Part Fibre Toxicol. 2013;10(1):5.
77. Cross LJ, Matthay MA. Biomarkers in acute lung injury: insights into the pathogenesis of acute lung injury. Crit Care Clin. 2011;27(2):355–77.
78. Yang D, Han Z, Oppenheim JJ. Alarmins and immunity. Immunol Rev. 2017;280(1):41–56.
79. Shi CS, Shenderov K, Huang NN, Kabat J, Abu-Asab M, Fitzgerald KA, et al. Activation of autophagy by inflammatory signals limits IL-1β production by targeting ubiquitinated inflammasomes for destruction. Nat Immunol. 2012;13(3):255–63.
80. Otsuki T, Maeda M, Murakami S, Hayashi H, Miura Y, Kusaka M, et al. Immunological effects of silica and asbestos. Cell Mol Immunol. 2007;4(4):261–8.
81. Re SL, Dumoutier L, Couillin I, Van Vyve C, Yakoub Y, Uwambayinema F, et al. IL-17A–Producing γδ T and Th17 Lymphocytes Mediate Lung Inflammation but Not Fibrosis in Experimental Silicosis. J Immunol. 2010;184(11):6367–77.
82. Chen Y, Li C, Weng D, Song L, Tang W, Dai W, et al. Neutralization of interleukin-17A delays progression of silica-induced lung inflammation and fibrosis in C57BL/6 mice. Toxicol Appl Pharmacol. 2014;275(1):62–72.
83. Skuland T, Låg M, Gutleb AC, Brinchmann BC, Serchi T, Øvrevik J, et al. Pro-inflammatory effects of crystalline- and nano-sized non-crystalline silica particles in a 3D alveolar model. Part Fibre Toxicol. 2020;17(1):13.
84. Breznan D, Das DD, O'Brien JS, MacKinnon-Roy C, Nimesh S, Vuong NQ, et al. Differential cytotoxic and inflammatory potency of amorphous silicon dioxide nanoparticles of similar size in multiple cell lines. Nanotoxicology. 2017;11(2):223–35.
85. Dong J, Ma Q. Type 2 immune mechanisms in carbon nanotube-induced lung fibrosis. Front Immunol. 2018;9:1120.
86. Wick G, Grundtman C, Mayerl C, Wimpissinger T-F, Feichtinger J, Zelger B, et al. The immunology of fibrosis. Annu Rev Immunol. 2013;31:107–35.
87. Barbarin V, Xing Z, Delos M, Lison D, Huaux FJAJoP-LC, Physiology M. Pulmonary overexpression of IL-10 augments lung fibrosis and Th2 responses induced by silica particles. Am J Physiol Lung Cell Mol Physiol 2005;288(5):L841-L8.
88. Brandenberger C, Rowley NL, Jackson-Humbles DN, Zhang Q, Bramble LA, Lewandowski RP, et al. Engineered silica nanoparticles act as adjuvants to enhance allergic airway disease in mice. Part Fibre Toxicol. 2013;10:26.
89. Swiercz R, Hałatek T, Stetkiewicz J, Wąsowicz W, Kur B, Grzelińska Z, Majcherek W. Toxic effect in the lungs of rats after inhalation exposure to benzalkonium chloride. Int J Occup Med Environ Health. 2013;26(4):647–56.
90. Bernstein JA, Stauder T, Bernstein DI, Bernstein IL. A combined respiratory and cutaneous hypersensitivity syndrome induced by work exposure to quaternary amines. J Allergy Clin Immunol. 1994;94(2 Pt 1):257–9.

91. Keane MP, Strieter RM. The importance of balanced pro-inflammatory and anti-inflammatory mechanisms in diffuse lung disease. Respir Res. 2002;3(1):5.
92. Le TT, Karmouty-Quintana H, Melicoff E, Le TT, Weng T, Chen NY, et al. Blockade of IL-6 Trans signaling attenuates pulmonary fibrosis. J Immunol (Baltimore, Md: 1950). 2014;193(7):3755–68.
93. Fitzgerald SM, Chi DS, Hall HK, Reynolds SA, Aramide O, Lee SA, et al. GM-CSF induction in human lung fibroblasts by IL-1 β, TNF-α, and macrophage contact. J Interferon Cytokine Res. 2003;23(2):57–65.
94. Lang DS, Schocker H, Hockertz S. Effects of crocidolite asbestos on human bronchoepithelial-dependent fibroblast stimulation in coculture: the role of IL-6 and GM-CSF. Toxicology. 2001;159(1–2):81–98.
95. Mor F, Quintana FJ, Cohen IR. Angiogenesis-inflammation cross-talk: vascular endothelial growth factor is secreted by activated T cells and induces Th1 polarization. J Immunol (Baltimore, Md: 1950). 2004;172(7):4618–23.
96. Fei M, Bhatia S, Oriss TB, Yarlagadda M, Khare A, Akira S, et al. TNF-α from inflammatory dendritic cells (DCs) regulates lung IL-17A/IL-5 levels and neutrophilia versus eosinophilia during persistent fungal infection. Proc Natl Acad Sci USA. 2011;108(13):5360–5.
97. Ullah R, Deb BK, Mollah MYA. Synthesis and characterization of silica coated iron-oxide composites of different ratios. Int J Compos Mater. 2014;4(2):135–45.
98. Bieseki L, Bertell F, Treichel H, Penha FG, Pergher SBC. Acid treatments of montmorillonite-rich clay for Fe removal using a factorial design method. Mater Res. 2013;16(5):1122–7.
99. Munasir M, Triwikantoro T, Zainuri M, Darminto D. Synthesis of SiO_2 nanopowders containing quartz and cristobalite phases from silica sands. Mater Sci Pol. 2015;33(1):47–55.
100. Porter DW, Ye J, Ma J, Barger M, Robinson VA, Ramsey D, et al. Time course of pulmonary response of rats to inhalation of crystalline silica: NF-kappa B activation, inflammation, cytokine production, and damage. Inhalation Toxicol. 2002;14(4):349–67.
101. Napierska D, Thomassen LC, Lison D, Martens JA, Hoet PH. The nanosilica hazard: another variable entity. Part Fibre Toxicol. 2010;7(1):39.
102. Morishige T, Yoshioka Y, Inakura H, Tanabe A, Yao X, Narimatsu S, et al. The effect of surface modification of amorphous silica particles on NLRP3 inflammasome mediated IL-1β production. ROS Prod Endosomal Rupture Biomater. 2010;31(26):6833–42.
103. Collins AR, Annangi B, Rubio L, Marcos R, Dorn M, Merker C, et al. High throughput toxicity screening and intracellular detection of nanomaterials. Wiley Interdiscip Rev Nanomed Nanobiotechnol. 2017;9(1):e1413.
104. Landsiedel R, Ma-Hock L, Wiench K, Wohlleben W, Sauer UG. Safety assessment of nanomaterials using an advanced decision-making framework, the DF4nanoGrouping. J Nanopart Res. 2017;19(5):171.
105. CRC Handbook of Chemistry and Physics. 92nd Edition. Anticancer Research. 2012;32(5):2220-.

Publisher's Note